Int J Earth Sci (Geol Rundsch) (2016) 105:1741–1760
DOI 10.1007/s00531-016-1343-y

ORIGINAL PAPER

# Numerical models of mantle lithosphere weakening, erosion and delamination induced by melt extraction and emplacement

**Herbert Wallner**[1] · **Harro Schmeling**[1]

Received: 19 July 2015 / Accepted: 25 May 2016 / Published online: 7 June 2016


**Abstract** Continental rifting caused by extension and heating from below affects the lithosphere or cratons in various ways. Volcanism and melt intrusions often occur along with thinning, weakening and even breaking lithosphere. Although mechanical necking models of the lithosphere are often applied, the aspects of melting and the implications due to melt transport and emplacement at shallower depths are not well understood. A two-phase flow approach employing melt extraction and shallow emplacement associated with thermal weakening is developed and compared with observations. The results of this comparison indicate the importance of partial melts and an asthenospheric magma source for increasing the rising rate of the lithosphere–asthenosphere boundary during extension. Thermomechanical physics of visco-plastic flow is approximated using the Finite Difference method with Eulerian formulation in 2D. The conservation of mass, momentum and energy equations are solved for a multi-component (crust–mantle) and two-phase (melt–matrix) system. Rheology is temperature- and stress-dependent. In consideration of depletion and enrichment melting and solidification are controlled by a simplified linear binary solid solution model. Melt is extracted and emplaced in predefined depth regions (emplacement zones) in the lithospheric mantle and crust. The Compaction Boussinesq Approximation was applied; its validity was tested against the Full Compaction formulation and found fully satisfactory for the case of sublithospheric melting models. A simple model guided by the geodynamic situation of the Rwenzori region typically results in updoming asthenosphere with melt-assisted erosion of the lithosphere's base. Even with a conservative approach for a temperature anomaly melting alone doubles the lithospheric erosion rate in comparison with a model without melting. With melt extraction and intrusion lithospheric erosion and upwelling of the lithosphere–asthenosphere boundary speeds up by a factor 3–4. In an extreme case, delamination may occur if weakening fully decouples a hanging mantle block. Models with an emplacement zone of up to approximately 70 km agree well with observations, especially for a concept based on seismological and petrological data.

**Keywords** Dynamics of crust and mantle · Continental tectonics · Lithospheric extension · Rifting process · Viscous two-phase flow · Melting · Rwenzori Mountains

## Introduction

Extension and thinning of cratonic lithosphere followed by continental rifting is a fundamental plate tectonic process on earth (Buck 2007). Often rifting is assisted by a plume impinging at the base of the lithosphere. Although this scenario is geologically and geophysically well documented for some cases, such as the East African Rift System (EARS) (Foley 2008; Koptev et al. 2015), the underlying physics is not well understood. Particularly, an understanding of the relationship between melting within the asthenosphere, the rise and emplacement of melts upwards to shallower depths (Schmeling and Wallner 2012; Sobolev et al. 2011) and the resulting updoming of the

**Electronic supplementary material** The online version of this article (doi:10.1007/s00531-016-1343-y) contains supplementary material, which is available to authorized users.

✉ Herbert Wallner
wallner@geophysik.uni-frankfurt.de

[1] Institut für Geowissenschaften, Goethe-Universität, Altenhöferallee 1, 60438 Frankfurt am Main, Germany

lithosphere–asthenosphere boundary (LAB) is insufficient. While thermal erosion of the lithospheric base has been discussed for a long time (e.g., Yuen and Fleitout 1985), unresolved questions include the relationships between the amount of lithospheric extension, the magma-assisted erosion from below and the mechanical thinning of the lithosphere. Recent studies on continental extension with thinning and erosion of lithosphere were conducted, e.g., by T. Gerya's group (Liao and Gerya 2014, 2015; Liao et al. 2013; Gerya 2014) where magma-related processes are modeled in a simplified way. Simplified models of how magma and heat are transported into shallower levels of a rifting craton and erode and weaken the lithosphere have been presented by Schmeling and Wallner (2012). Spiegelman and McKenzie described the theoretical bases of melt extraction (Spiegelman and McKenzie 1987; Spiegelman 1993) with applications in models mostly on mid-ocean ridges or mantle wedges above subducting slabs (e.g., Kelemen 2000; Hebert and Montési 2011; Gerya and Meilick 2011; Katz and Weatherley 2012; Gregg et al. 2012). However, the systematics of this melt-assisted erosion up to the end-member case that the erosion level reaches the Moho and, in extreme cases, the generation of plate decoupling or delamination of the associated mantle lithosphere (Wallner and Schmeling 2011 and references therein; Bajolet et al. 2012), have not been studied. To gain more insight regarding the physics behind these processes, we numerically modeled them guided by geodynamic constraints from a characteristic section of the EARS, namely the Rwenzori Mountains (RWZ) region (Wallner and Schmeling 2010). Therefore, we briefly describe the geodynamic situation of this region. Nevertheless, the studied processes and the quantified geodynamic mechanism may be generalized and applied to other scenarios.

The core of a continent is often formed by a craton with a lithosphere up to 250 km in thickness. Cratons are less dense than the surrounding mantle material. Due to their age, cratons are relatively cold, and as a consequence, stiff, and stable over long periods (Lenardic et al. 2003). Special conditions and combinations of mechanisms are needed to break a continent and initiate rifting (Buck 2007). In the case of the EARS, this breaking or rifting appears to follow old suture zones called mobile belts which separate the individual cratons. The rate of rifting is constrained by plate kinematics known from geology as a function of time or, more recently, from GPS measurements (Calais et al. 2006; Stamps et al. 2008). The mean drift rate estimated from the amount of extension with time (Wallner and Schmeling 2010) agrees with actual values obtained from GPS studies (Saria et al. 2014) of approximately 2 mm/a = 2 km/Ma and is nearly perpendicular to the Albertine rift axis.

As a characteristic feature of the western branch of the EARS, the Rwenzoris are an old Proterozoic crustal horst

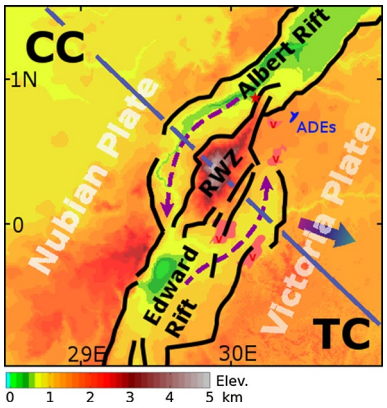


**Fig. 1** Top view of the geological situation of the Rwenzori Mountains (RWZ). The *color map* shows the topography of the Albertine Rift, part of the western branch of EARS between the Congo craton (CC) and the Tanzania craton (TC). The main tectonic features are indicated: major rift faults, drift rate of 2 mm/a (*thick arrow*), volcanics (*pink patches* with V), hot springs (*red star*), positions of anomalous deep earthquakes (ADEs, *blue*) and the profile for a cross section (Fig. 10). The horst of RWZ is encircled by the approaching tips of the Lake Albert and Lake Edward rift segments; *broken violet arrows* imply the evolution of the rift tips

situated between active segments of this rift. It is nearly completely encircled by the southward-propagating Lake Albert rift and the northward-migrating Lake Edward rift. Relative to its local size of 50 × 120 km, the top elevation of the Rwenzoris reaches an extreme height of more than 5 km (Figs. 1, 10) (Koehn et al. 2010; Link et al. 2010). By contrast, the Moho depth beneath the massif is approximately 24 km (i.e., at the typical rift level), while the Moho depth of the adjacent Tanzania and Congo craton is typically 30–40 km (Wölbern et al. 2010; Gummert et al. 2015). Thus, the crustal root of the Rwenzori Mountains is missing. The depth of the LAB has been constrained at 140 km beneath the rift, deepening to 210 km beneath the Tanzania craton (Wölbern et al. 2012). Interpreted observations are compiled in Fig. 10.

The second ingredient of the process, besides extension, is a plume that interacts with the craton and assists the rifting process. Several studies on seismic tomography and vertical phase-boundary shifts within the transition zone support the assumption that a mantle plume exists beneath the Tanzanian craton (Huerta et al. 2009; Weeraratne et al. 2003; Mulibo and Nyblade 2013). Kimberlites in the innermost part of the craton and recent erupting carbonatites along the craton margin (Foley et al. 2012) also indicate elevated temperatures beneath the craton. The Tanzanian craton hampers the further rise of the plume, and its low viscous head spreads under the keel following the negative topography of the craton's base. Tomographic images (Mulibo and Nyblade 2013) suggest that its branches reach the craton margin and ascend

at its edges, intrude the surrounding weak asthenosphere and heat it up. The existence of the eastern and western branch of EARS confirms this perception. Focusing again on the western branch around the Rwenzori Mountains, we encounter the situation that plume material could rise into the active rift segments east and west of the Rwenzori block and generate twin thermal anomalies approximately 50 km apart.

Now, we aim to constrain the associated asthenospheric temperatures. While excess plume temperatures prior to the interaction with the lithosphere are estimated at approximately 300 K (Zhong 2006), lateral spreading beneath the craton will reduce this figure. Low seismic velocities at a depth of 50 km beneath the western branch of the EARS have been interpreted in terms of excess temperatures of at least 130 K (Jakovlev et al. 2013). Thus, an excess asthenospheric temperature of approximately 150 K above the normal potential temperature is plausible for the sub-rift asthenosphere and agrees with the anomalous potential temperature estimate of the EARS of approximately 1400–1500 °C (Rooney et al. 2012). At such temperatures, sublithospheric convection is expected within the asthenosphere (Schmeling and Bussod 1996) and will be associated with lateral temperature variations on the order of 50–200 K over wavelengths on the order of 100 km, with lower values preferred at higher Rayleigh numbers (Schmeling and Marquart 1991, 1993). Clearly, such asthenospheric temperatures exceed the solidus temperature. In a more recent study, Till et al. (2010) conclude that even craton edge driven asthenospheric flow is sufficient to produce low-extent melts beneath the LAB. Link et al. (2010) report that the magmas of Toro-Ankole volcanism SE and near the Rwenzori Mountains originate from depths >150 km.

This study is part of the RiftLink project "Rift Dynamics, Uplift and Climate Change in Equatorial Africa" aimed at modeling deep processes concerning rift systems, with particular emphasis on the rifts around the Rwenzori Mountains. Indeed, new observations by other RiftLink teams underscore the importance of partial melts (see Fig. 10). Jakovlev et al. (2013) interpreted low P-wave velocity anomalies at a depth of 50 km beneath the rift that resulted from partial melts of 1–2 %. Wölbern et al. (2012) detected a seismic discontinuity within the mantle lithosphere beneath the rift at a depth of 50 km and interpreted it as the top of a melt infiltration front (MIF). At that depth, active ongoing intrusion may have been repeatedly revealed by an earthquake swarm at that anomalous depth (Lindenfeld and Rümpker 2011), which is marked as ADE (anomalous deep earthquake) in Figs. 1 and 10. The detection of a melt infiltration front has been supported by petrological arguments based on xenoliths (Link et al. 2010; Wölbern et al. 2012). A consequence of melt infiltration into shallower lithosphere will be thermal weakening.

An important part of the melt-induced thermal weakening concept is the requirement of rapid melt transport into the lithosphere. Geochemical arguments for fast melt transport through the subsolidus lithosphere are reviewed in the introduction in Schmeling (2006). Observations and the presence of volcanism (Toro-Ankole near Lake George, east of Rwenzori Mountains, Link et al. (2010)) suggest that there is rapid melt transport from beneath the lithosphere to the surface. Although the complete process of melt extraction and rise through the subsolidus lithosphere is not yet fully understood, Schmeling (2006) proposed a physical concept of episodic melt extraction in which the melt may form subvertical melt-rich channels due to its mechanical instability within the partially molten mantle region. Upon reaching a critical length, the melt may leave the partially molten region in the form of propagating dykes. Rather than invoking a critical length, many modeling approaches (including the present one) only use one critical melt extraction threshold of approximately 1 %. Fast melt transport through the lithosphere by dykes and/or veins is consistent with the observed SKS anisotropy subparallel to the rift axis (Homuth et al. 2014). Emplacement at a shallower level is consistent with the general picture that only roughly 10 % of the melt in extensional regions may be extruded (Crisp 1984). The remaining melt is emplaced at depth in the form of intrusions. A natural level of shallow magma emplacement is at the Moho and is known as crustal underplating (Thybo and Artemieva 2013). However, this may represent a late or final rifting stage. During the early phase, not all melts may reach such shallow levels, as suggested by the melt infiltration front at a depth of approximately 50–60 km. This discussion provides a rationale for treating the intrusion level in our physical model as a free parameter and for designing a series of numerical models for various emplacement zones, including the Moho level.

In Wallner and Schmeling (2010, 2011), rift-induced delamination has been proposed to explain some of the enigmatic observations around the Rwenzori block (Bahat and Mohr 1987). These explanations include extreme topography, old metamorphic and nearby young volcanic rocks, crustal thickness, and structural tectonics and seismicity. The models were based on ad hoc thermal initial conditions and neglected melting. The above discussion suggests that the delamination process may be incomplete around the Rwenzori block. Instead, lithosphere base erosion may still be acting in the northern parts. This hypothesis will be tested here by using more realistic models of the rise of the LAB on both sides of a lithospheric block that resembles the Rwenzori block. In contrast with the previous models of Wallner and Schmeling (2010, 2011), this approach will include melting and melt-induced thermal weakening of the lithosphere, as described for different scenarios

by Schmeling and Wallner (2012). Rift-induced delamination will only be an end-member case for the various melt extraction and redistribution scenarios considered here.

## Theoretical formulation of two-phase flow with melting and emplacement

The governing equations describing the dynamics of a two-phase material consisting of fluid (subscript f, here melt) and solid matrix (subscript s) in the high Prandtl number approximation (McKenzie 1984; Spiegelman and McKenzie 1987; Schmeling 2000) include the following equations for the conservation of the melt mass:

$$\rho_\mathrm{f}\left(\frac{\partial\varphi}{\partial t}+\nabla\cdot[\varphi\ \underline{v}_\mathrm{f}]\right)=\Gamma-\rho_\mathrm{f}\,q_\mathrm{extr}, \tag{1}$$

the matrix mass:

$$\rho_\mathrm{s}\left(\frac{\partial(1-\varphi)}{\partial t}+\nabla\cdot\left[(1-\varphi)\ \underline{v}_\mathrm{s}\right]\right)=-\Gamma \tag{2}$$

the momentum of the melt:

$$\underline{v}_\mathrm{f}-\underline{v}_\mathrm{s}=-\frac{k_\varphi}{\eta_\mathrm{f}\,\varphi}(\nabla P-\rho_\mathrm{f}\underline{g}), \tag{3}$$

the momentum of the matrix:

$$\rho\underline{g}-\nabla P+\nabla\cdot\underline{\underline{\tau}}=0, \tag{4}$$

and the energy of the melt and matrix mixture:

$$\rho c_\mathrm{p}\left(\frac{\partial T}{\partial t}+\underline{v}^\mathrm{T}\nabla T-\frac{\alpha}{c_\mathrm{p}}\underline{g}^\mathrm{T}\underline{v}\,T_\mathrm{abs}\right)=\nabla\cdot(k\nabla T)+\rho H+Q_\mathrm{Di}-L\Gamma+Q_\mathrm{intru}. \tag{5}$$

The quantities and some values are defined in Table 1. Pressure in the fluid and matrix skeleton are considered equal because it is assumed that no surface tension acts at the interface of solid matrix and fluid melt. During rapid ascent, melt and ambient matrix are not in thermal equilibrium and the energy equation should be divided into two coupled equations for melt and matrix, respectively. Using this approach, we avoid dealing with the complex and lesser known physics of fast melt transport and retain one heat equation for both phases by replacing rapid melt ascent with extraction and emplacement terms. Thus, melt extraction and emplacement are assumed to occur on a short timescale compared to the long timescale of matrix deformation, during which the temperatures of the melt and matrix are assumed to be at equilibrium.

The constitutive equations are given as follows:

$$\underline{\underline{\tau}}=\eta_\mathrm{s}\left(\nabla\underline{v}_\mathrm{s}+\nabla\underline{v}_\mathrm{s}^\mathrm{T}\right)+\left(\eta_\mathrm{b}-\frac{2}{3}\eta_\mathrm{s}\right)\underline{\underline{I}}\,\nabla\cdot\underline{v}_\mathrm{s}, \tag{6}$$

where the viscous stress tensor with $\nabla\underline{v}$ as the velocity gradient tensor and applying the dyadic or tensor product is often written as $\nabla\otimes\underline{v}$, where $\nabla\underline{v}^T=\underline{v}\otimes\nabla$ is its transpose, $\underline{\underline{\dot{e}}}=\frac{1}{2}\left(\nabla\underline{v}_\mathrm{s}+\nabla\underline{v}_\mathrm{s}^\mathrm{T}\right)$ is the strain rate tensor of the matrix and the permeability

$$k_\varphi=k_0\,\varphi^n. \tag{7}$$

The viscosities are typically functions of temperature, stress and pressure for earth materials, which result in nonlinear relationships. The linearized equation of state for density is given as

$$\rho=\rho_0\left(1-\alpha T-\frac{\rho_\mathrm{s}-\rho_\mathrm{f}}{\rho_\mathrm{s}}\varphi+\rho_{d|e}f\right) \tag{8}$$

where $\rho_{d|e}=\rho_\mathrm{dp}, f>0$ for depletion and $\rho_{d|e}=\rho_\mathrm{enr}, f<0$ for enrichment.

The Compaction Boussinesq Approximation (CBA) is used (see Schmeling 2000, 2006, and Appendix of electronic supplementary material), which essentially neglects density variations (other than buoyancy terms) and compaction for the matrix flow but incorporates compaction pressure when considering melt flow. The resulting dimensionless flow equations in 2D (dimensionless quantities are primed) (see also Schmeling 2000) are for the matrix

$$\left(\frac{\partial^2}{\partial x'^2}-\frac{\partial^2}{\partial z'^2}\right)\left[\eta_\mathrm{s}'\left(\frac{\partial^2\Psi'}{\partial x'^2}-\frac{\partial^2\Psi'}{\partial z'^2}\right)\right]+4\frac{\partial^2}{\partial x'\partial z'}\left[\eta_\mathrm{s}'\frac{\partial^2\Psi'}{\partial x'\partial z'}\right]=Ra\frac{\partial T'}{\partial x'}+Rm\frac{\partial\varphi}{\partial x'}+Rd\frac{\partial f}{\partial x'} \tag{9}$$

and the melt

$$\underline{v}_\mathrm{f}'-\underline{v}_1'=\frac{Rm}{Rt}\varphi^{n-1}(1-\varphi)\underline{e}_z-\frac{\varphi^{n-1}}{Rt}\left(\nabla'\cdot\left[\eta_\mathrm{s}'\left(\nabla'\underline{v}_1'+\nabla'\underline{v}_1'^{\,T}\right)\right]+\nabla'\left[\eta^*\nabla'\cdot\underline{v}_\mathrm{s}'\right]\right) \tag{10}$$

where $\Psi$ is the stream function and is defined by

$$v_{1x}=\frac{\partial\Psi}{\partial z},\quad v_{1z}=-\frac{\partial\Psi}{\partial x} \tag{11}$$

where $\underline{v}_1$ is the divergence-free part of the matrix velocity field, $\underline{v}_\mathrm{s}$, $\eta^*=\eta_\mathrm{b}'$ in the CBA, and $\eta^*=\eta_\mathrm{b}'-2\,\eta_\mathrm{s}'/3$ in the Full Compaction formulation. In the CBA, the last term in (10) is determined from Eqs. (1) and (2):

$$\nabla\cdot\underline{v}_\mathrm{s}=\Gamma\left(\frac{\rho_\mathrm{s}-\rho_\mathrm{f}}{\rho_0^2}\right)-q_\mathrm{extr}-\nabla\cdot\left[\varphi\left(\underline{v}_\mathrm{f}-\underline{v}_\mathrm{s}\right)\right]. \tag{12}$$

A typical model with the Full Compaction formulation was rerun to test the validity of the CBA for the sublithospheric melting and extraction cases (see Appendix of electronic supplementary material).

**Table 1** Definitions and values of various quantities

| Symbol | Meaning and values |
|---|---|
| $c_{\mathrm{freeze}}$ | Case-dependent factor for melting degree difference |
| $c_{\mathrm{p}}$ | Heat capacity at constant pressure (1300 J/(kg K)) |
| $f$ | Melting degree (>0 for depletion, <0 in case of enrichment) |
| $_{\mathrm{f}}$ (subscript) | Fluid |
| $f_{\mathrm{m}}$ | Melting function |
| $g$, $\underline{g}$ | Gravitational acceleration (10 m/s$^2$), gravity vector |
| $h$ | Thickness of the model (200 km) |
| $H$ | Radiogenic heat generation ($5.86 \times 10^{-12}$ W/kg + $0.18 \times 10^{-10}$ W/kg·exp(z/30 km) |
| $k$ | Heat conductivity (4.42 W/(m K)) |
| $k_\varphi$, $k_0$ | Permeability, constant of the permeability–porosity relation ($10^{-9}$ m$^2$) |
| $L$ | Latent heat (400 kJ/kg) |
| $n$ | Power of the permeability–porosity relation (3) |
| $P$ | (Fluid) pressure |
| $q_{\mathrm{extr}}$, $q_{\mathrm{intru}}$ | Specific volumetric rate of melt extraction and melt emplacement |
| $Q_{\mathrm{Di}}$ | Dissipation rate |
| $Q_{\mathrm{intru}}$ | Intrusional heat rate due to melt extraction |
| $_{\mathrm{s}}$ (subscript) | Solid |
| $t$ | Time |
| $T$, $\Delta T$, $T_{\mathrm{abs}}$ | Temperature, scaling temperature (1000 K), absolute temperature |
| $T_{\mathrm{sol}}$, $T_{\mathrm{liq}}$ | Solidus and liquidus temperature ($T_{\mathrm{sol}} = 1403$ K–2.5 K/km $\cdot z$, $T_{\mathrm{liq}} = T_{\mathrm{sol}} + 600$ K) |
| $\underline{v}$, $\underline{v_{\mathrm{s}}}$, $\underline{v_{\mathrm{f}}}$, $\underline{v_{\mathrm{segr}}}$ | Velocity, $\underline{v} = (1-\varphi)\underline{v_{\mathrm{s}}} + \varphi\,\underline{v_{\mathrm{f}}}$, solid, fluid, segregation velocity |
| $x$, $z$ | Horizontal, vertical coordinate, positive upwards, origin at earth's surface |
| $X$ | Specific mass of a component |
| $\alpha$ | Volumetric thermal expansivity ($3.7 \times 10^{-5}$ K$^{-1}$) |
| $\Gamma$ | Rate of melt generation (melt mass per volume and time) |
| $\eta_{\mathrm{b}}$, $\eta_{\mathrm{s}}$, $\eta_{\mathrm{f}}$, $\eta_0$ | Effective bulk ($10^{22}$ Pa s) and shear viscosities of the (porous) matrix $\eta_{\mathrm{s}} = \eta_{\mathrm{s}}(\underline{\underline{\tau}}, T, \sigma_Y)$, fluid (melt) viscosity ($3 \times 10^2$ Pa s), scaling viscosity ($10^{21}$ Pa s) with a $10^{\pm 4}$ cutoff |
| $\kappa$ | Thermal diffusivity ($10^{-6}$ m$^2$/s) |
| $\rho$, $\rho_0$, $\rho_{\mathrm{s}}$, $\rho_{\mathrm{f}}$ | Density, scaling density (3400 kg/m$^3$), solid density ($\rho_s = \rho_0$), melt density (3012 kg/m$^3$). The scaling density is set to 2628 kg/m$^3$ in the upper crust, to 3100 kg/m$^3$ in the lower crust |
| $\rho_{\mathrm{dp}}$, $\rho_{\mathrm{enr}}$ | Depletion density (3111 kg/m$^3$), enrichment density (2788 kg/m$^3$ above and 3740 kg/m$^3$ below 40 km depth) |
| $\underline{\underline{\tau}}$ | Viscous stress tensor |
| $\varphi$, $\varphi_{\mathrm{extr}}$ | Melt fraction, melt extraction threshold (1 %) |
| $\Psi$ | Stream function |
| $\chi$ | Irrotational velocity potential |

The thermal, melt and depletion Rayleigh numbers (*Ra, Rm, Rd*, respectively) and the melt retention number, *Rt*, are defined as follows:

$$Ra = \frac{\rho_0 g \alpha \Delta T\, h^3}{\eta_0 \kappa}, \quad Rm = \frac{(\rho_0 - \rho_{\mathrm{f}})\, g\, h^3}{\eta_0 \kappa},$$
$$Rd = \frac{\left(\rho_0 - \rho_{d|e}\right) g\, h^3}{\eta_0 \kappa}, \quad Rt = \frac{\eta_{\mathrm{f}} h^2}{\eta_0 k_0}. \tag{13}$$

The heat conductivity is assumed constant, and radiogenic heating is assumed to decrease exponentially with depth.

Phase changes, melting and freezing of rocks influence mineralogy, petrology and physical properties. During partial melting the rock matrix loses basaltic components which go to the melt. The melt will be advected with respect to the matrix, extracted, or intruded elsewhere and where the melt solidifies the matrix becomes enriched in basaltic component. These complex processes are subsumed by $f$ as degree of melting of the matrix, or depletion ($f > 0$) or enrichment ($f < 0$) of basaltic component, summing up all generated or solidified melt fractions following a matrix volume element when summed. Depletion and enrichment of the rock are advected with the matrix and is varied due to melting, freezing or intrusion according to

$$\frac{\partial f}{\partial t} + \underline{v_{\mathrm{s}}} \cdot \nabla f = \frac{\Gamma}{\rho_{\mathrm{f}}} - q_{\mathrm{intru}}. \tag{14}$$

The term $q_{\text{intru}}$ is discussed below. Depletion and enrichment are related to density changes and thus correspond to positive or negative buoyancy forces that drive the flow in addition to thermally induced density changes. In addition, for enrichment there is a phase boundary at a depth of 40 km. Above this depth, melt freezes to a basalt-like low-density component, and below this depth, melt solidifies into an eclogite-like material with higher density (see Table 1).

Melting and solidification are modeled using a simplified binary solid solution model that assumes a solid solution of two components, $A$ and $B$, with specific masses, $X_A$ and $X_B$, respectively (Fig. 2). The solidus and liquidus curves are assumed to be parallel straight lines for convenience; higher degrees of melting or not more realistic melting laws should consider a composition-dependent difference of $T_{\text{liq}} - T_{\text{sol}}$. If the initial composition of a volume element is given as $X_0$, melting will begin once $T$ reaches $T_{\text{sol}}$ ($X_0$). If no melt leaves the element, increasing the temperature by $\delta T$ will generate melt with a composition $X_{\text{m}}$. According to the lever rule, the melt fraction is $(X_{\text{s}} - X_0)/(X_{\text{s}} - X_{\text{m}})$. The melting degree (or depletion/enrichment) of the matrix is defined as

$$f = \frac{X_{\text{s}} - X_0}{X_{\text{s}} - X_{\text{m}}} \tag{15}$$

and is still identical to the melt fraction. If the melt with composition $X_{\text{m}}$ leaves the volume element by percolation or extraction, the composition of the element changes by $\delta X$ and the solidus temperature changes by $\delta T_{\text{sol}}$ to the new solidus temperature, $T_{\text{sol}}(X)$. Because the actual melt fraction at the new composition $X$ is given by $\varphi = (X_{\text{s}} - X)/(X_{\text{s}} - X_{\text{m}})$ and the depletion remains the same, simple geometrical considerations can be used to obtain changes of the solidus temperature $\delta T_{\text{sol}} = (f - \varphi)\,(T_{\text{liq}} - T_{\text{sol}})$. Thus, the composition-dependent solidus and liquidus temperatures are given by $T_{\text{sol}}(z, f) = T_{\text{sol}}(z, f = 0) + (f - \varphi)\,\Delta T_{\text{liso}}$ with $\Delta T_{\text{liso}} = T_{\text{liq}} - T_{\text{sol}}$, and $T_{\text{liq}}(z, f) = T_{\text{sol}}(z, f) + \Delta T_{\text{liso}}$. The essential distinction between $f$ and $\varphi$ is: the melting degree $f$ concerns the actual composition of the matrix with respect to the original composition at the onset of melting; in contrast the melt fraction $\varphi$ specifies the actual amount of melt in a volume unit, sometimes called melt porosity. At any composition $X$ and temperature $T$ above the $X$-dependent solidus temperature, the rate of melt generation or freezing can be determined by considering the total temperature derivative with time following the volume element and the temporal change of the pressure-dependent solidus and liquidus temperatures due to vertical flow velocity.

$$\Gamma = \begin{cases} \rho_{\text{f}} \left.\dfrac{\partial f_{\text{m}}}{\partial T}\right|_P \left(\dfrac{\partial T}{\partial t} + \underline{v}^{\text{T}} \nabla T\right) & \\ \quad + \rho_{\text{f}} \left.\dfrac{\partial f_{\text{m}}}{\partial P}\right|_T \rho \underline{g}^{\text{T}} \underline{v} & \text{for} \quad T_{\text{sol}}(z,f) < T < T_{\text{liq}}(z,f) \\ 0 & \text{elsewhere} \end{cases} \tag{16}$$

where $f_{\text{m}}$ ($T$, $P$) is the temperature-, pressure- and depletion-dependent melting function of peridotite. This melting function may be taken from parameterizations given, e.g., by Katz et al. (2003), and here we simply take a linear parameterization $f_{\text{m}} = (T - T_{\text{sol}}\ (z,\ f))/\Delta T_{\text{liso}}$ for $T_{\text{sol}} < T < T_{\text{liq}}$, else $f_{\text{m}} =$ constant (0 or 1).

The above set of equations is solved as follows for one time step: Given the temperature, the melt and the melting degree fields, Eq. (9) and the nonlinear viscosity–velocity relation of the matrix are solved iteratively for $\Psi$, $\underline{v_1}$, $\eta_{\text{s}}$ and $\underline{\underline{\tau}}$ by Finite Differences involving Eqs. (6), (8), (11) and (13) and the strain rate tensor. Then, Eqs. (1), (10) and (12) are iteratively solved for segregation velocity, $\underline{v_{\text{segr}}} = \underline{v_{\text{f}}} - \underline{v_{\text{s}}}$, and the melt fraction $\varphi$ at the new time step using implicit Finite Differences and an upwind scheme. After advecting $f$ by solving Eq. (14) the new temperature, melt generation rate $\Gamma$, extraction and intrusion rates are calculated by solving the temperature Eq. (5) by an ADI scheme using upwind, and Eqs. (16–19), respectively. Now, all quantities are known at the new time step, and the procedure can be repeated for the next time step.

Up to now fast melt transport, including melting and freezing, was not self-consistently modeled in rifting setups because of different timescales. We replace this mechanism by extraction of melt from the source region and intrusion at different locations and include the energy transfer. More specifically, melt extraction is modeled by taking out all generated melt that exceeds a certain extraction threshold of $\varphi_{\text{extr}}$ in the melt source region. The extraction rate from Eq. (1) thus is given by

$$q_{\text{extr}} = \begin{cases} 0 & \text{for} \quad \varphi < \varphi_{\text{extr}} \\ \dfrac{\Gamma}{\rho_{\text{f}}} - \varphi_{\text{extr}} \nabla \cdot \underline{v_{\text{f}}} & \text{for} \quad \varphi = \varphi_{\text{extr}} \end{cases}. \tag{17}$$

The case $\varphi > \varphi_{\text{extr}}$ does not occur because melt above the limit is extracted.

Once the melt is emplaced within a certain shallower intrusion depth interval, which we call emplacement zone (EZ), the magma either completely freezes (if the temperature of the emplacement zone is below its solidus temperature) or partially solidifies leaving a remaining melt fraction relative to its original, fully molten volume of $\varphi_{\text{intru}} = (X_{\text{s}} - X_{\text{m-source}})/(X_{\text{s}} - X_{\text{m}})$ according to the lever rule. Here, $X_{\text{s}}$ and $X_{\text{m}}$ are compositions of the solid and melt in the emplacement zone, respectively, and $X_{\text{m-source}}$ is the composition of the melt in the source region. Assuming the same simplified binary solid solution model as above (Fig. 2) and using Eq. (16) for both the source and emplacement zones, the terms $X_{\text{s}}$ and $X_{\text{m-source}}$ can be expressed in terms of the depletion of the source region, $f_{\text{source}}$, and emplacement zone, $f_{\text{empl}}$. The latter is negative in the case of enrichment. Consequently, $\varphi_{\text{intru}} = 1 - f_{\text{source}} + f_{\text{empl}}$. Thus, the solidifying fraction of the emplaced magma is

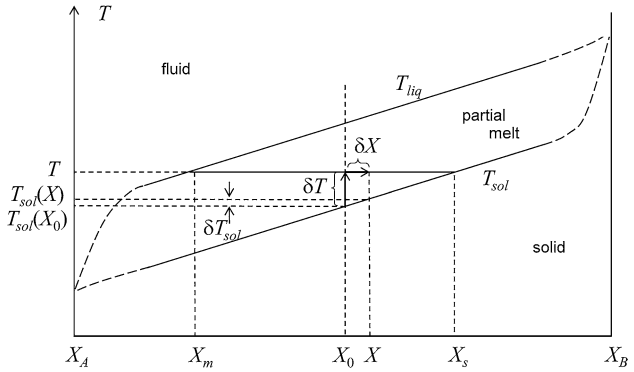


**Fig. 2** Melting model for a two (*A, B*)-component solid solution. The Lever rule divides a composition $X_0$ into melt ($X_m$) and solid ($X_s$) composition for temperature increase $\delta T$. The solidus, $T_{sol}$, changes if an element's composition is altered ($\delta X$) by extraction of melt

equal to $f_{source} - f_{empl}$. Using this result, we can determine the amount of intrusional heating rate due to the release of internal and latent heat during complete or partial freezing (see also Schmeling and Marquart 2008) as follows:

$$Q_{intru} = \rho_s c_p \left( T_{source} - T + c_{freeze} \frac{L}{c_p} \right) \cdot q_{intru}$$
$$\text{with} \quad c_{freeze} = \begin{cases} f_{source} - f_{empl} & T \geq T_{sol} \\ 1 & T < T_{sol} \end{cases} \tag{18}$$

where $T_{source}$ and $T$ are the temperatures in the source and emplacement regions, respectively, $T_{sol}$ is the solidus temperature in the emplacement zone, and

$$q_{intru} = \rho_f \int_{h_{extr}} q_{extr} dz / (h_{intru} \rho_{enr}) \tag{19}$$

is the volumetric intrusion rate of the emplaced magma (=0 outside the intrusion zone), which is calculated from the integrated extraction rate of the source region as shown below. Here, $h_{extr}$ and $h_{intru}$ are the depth intervals at which extraction and intrusion take place, respectively. It is reasonable to assume that intrusional emplacement only occurs in the subsolidus part of the lithosphere. Thus, $c_{freeze}$ is always equal to 1.

The term $q_{intru}$ is calculated by redistributing the total amount of extracted melt per time evenly within the EZ. No lateral magma transport during extraction is assumed (i.e., each melt particle is emplaced in the column of the emplacement zone exactly above the position where it is extracted). In addition, the term $q_{intru}$ changes the degree of depletion or enrichment at the position of intrusion (see Eq. 14).

Within the framework of the Compaction Boussinesq Approximation, this formulation ensures mass conservation within the model. Local volume changes due to extraction and emplacement are only included in the Full Compaction formulation (Appendix of electronic supplementary material).

## Model setup

The setup is an attempt to keep the model simple and general, while allowing the results to transfer to the specific situation of the Rwenzoris, which we regard as a typical case of an extensional lithosphere with an eroding LAB, melt emplacement and lithospheric weakening. Experience from one-phase physics models testing rift-induced delamination (Wallner and Schmeling 2010, 2011) is incorporated into the design of the model. The definition of the model contains geometry, boundary and initial conditions, the rheology of matrix and melt, melt curves, and extraction and emplacement parameters. The parameter values are given in Table 1, and most features are shown in Fig. 3.

### Geometry

The elongated structure of the EARS and the Rwenzoris represents the rifting margin of a craton and allows the space dimension to be reduced to 2D. In addition, the fair degree of symmetry allows the model width to be restricted to half of the geometry, resulting in a square box of 200 × 200 km. Laterally, the outer margin is far enough away to avoid influencing essentially the melt-induced dynamics near the rift axis through boundary effects. Vertically, the model reaches into the asthenosphere. It is composed of three layers, an upper and lower crust (20 and 15 km, respectively) and a third layer beneath the mantle. The mechanical structure is defined by viscous and plastic rheology. The model and its boundary conditions are compiled in Fig. 3.

### Resolution

The spatial resolution for the stream function is 101 × 101 grid points (i.e., a spacing of 2 km) and that for the energy and melt equations is 401 × 401. Material properties, such as density and viscosity, are advected by 1001 × 1001 markers. Higher resolutions of up to a factor of 2 have been tested and converge at similar solutions. The temporal resolution depends on the flow velocities following the Courant criterion, which begins with a time increment of 100 a and is limited by 50 ka.

### Boundary conditions

Extensional plate kinematics is realized as a material outflow boundary condition at the right boundary. A constant

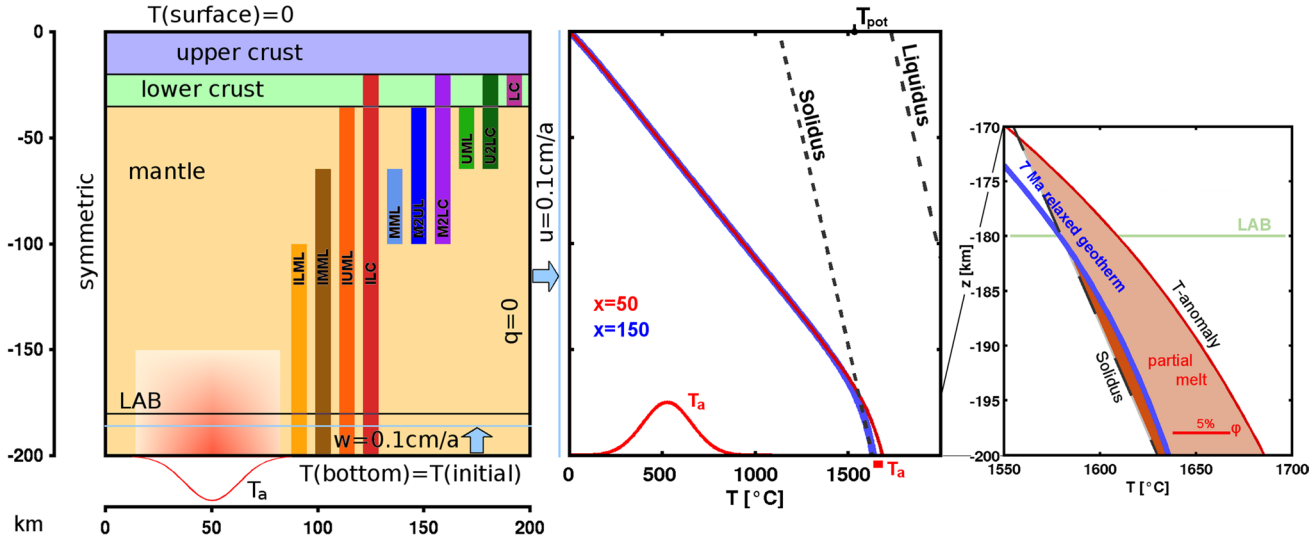


**Fig. 3** *Left* model geometry, structure, boundary (BC) and initial conditions (IC) with a series of emplacement zone variations (see Table 2). *Mid* initial geotherm away (*blue*) and through the temperature (*T*-) anomaly (*red*). This model is constructed from a lithospheric gradient crossing the adiabate at $z = -180$ km (LAB) and relaxation for 7 Ma by one-phase physics. Melt temperature curves are shown as *dashed lines*. The bottom temperature is just above the solidus $T_{sol}$, which is initially generating a melt fraction approximately 1 % away from the anomaly. The temperature anomaly $T_a$ is defined as a Gaussian-shaped function as bottom BC beneath the future rifts. The maximum excess amplitude of this function is 50 K. Thus, the initial fraction at the *T*-anomaly is 9 %. *Right* close-up near the *T*-anomaly. The high melt fraction is extracted immediately in the first time step

velocity of $v_x$ ($x = 200$ km, $-200 < z < 0$ km) = 1 mm/a is prescribed. Due to mass conservation the outflow is balanced by an inflow through the bottom ($v_z$ ($0 < x < 200$ km, $z = -200$ km) = $v_x$). No flow occurs through the top and left boundary, and the latter is the symmetry axis. Tangentially free slip is applied to all boundaries. Thus, the top, which is interpreted as the surface, is not vertically free. Checking the influences of these boundary conditions with "sticky air" models (see also Crameri et al. 2012) revealed only minor effects.

The thermal boundary conditions include zero conductive heat flux at the side, $T = 0$ °C at the surface and $T = T_{bot} = 1636$ °C at the bottom, with an additional anomaly mimicking lateral variations in a convecting asthenosphere. This anomaly is defined by a Gaussian function with a maximum excess amplitude of $T_a = 50$ K, a width of 25 km and an offset of 50 km from the symmetry axis. This temperature profile forms the bottom boundary condition when added to $T_{bot}$.

## Initial condition

As initial temperature an almost linear background geotherm in the thick lithosphere is assumed. Its "cratonic" thickness before rifting is set to 180 km because the Congo and Tanzanian cratons are still connected north of the Rwenzoris (Link et al. 2010). The asthenosphere's temperature is assumed to be adiabatic, with an intercept at $z = 0$ given by the potential temperature $T_{pot} = 1533$ °C. This value is close to the higher estimate for the EARS (Rooney et al. 2012, see chapter 1) and was chosen so that the melting temperature intersects the adiabat near the model's bottom to generate a melt fraction of approximately 1 % (see close-up in Fig. 3). Because combining the lithospheric and asthenospheric temperature gradients provides an artificial kink at the initial model LAB (which would generate melt), the geotherm is conductively relaxed for 7 Ma so that the LAB temperature decreases below the solidus. Finally, to avoid a step above the temperature anomaly at the bottom, the anomaly decays vertically linearly up to −150 km in the initial temperature field (see Fig. 3).

## Rheology

As discussed by Wallner and Schmeling (2011), the rheology is assumed temperature-, pressure- and stress-dependent based on laboratory measurements of Westerly Granite in the upper crust, clinopyroxenite in the lower crust (Kirby and Kronenberg 1987) and dry Aheim Dunite in the mantle (Chopra and Paterson 1984). Strength-limiting brittle behavior is included using a Byerlee's law-based depth-dependent plastic viscosity. The yield stress $\sigma_Y$ of the lower crust is reduced by lowering the pore pressure factor $1 - P_{fl}/P_{Lith}$ to 0.01, where $P_{fl}$ and $P_{Lith}$ are the fluid and lithostatic pressures, respectively.

**Table 2** Model series with EZ variations

| Model | $z_1$ (km) | $z_2$ (km) | Acronym's meaning |
|---|---|---|---|
| ILML | −200 | −100 | Into lower mantle lithosphere |
| IMML | −200 | −70 | Into mid-mantle lithosphere |
| IUML | −200 | −35 | Into upper mantle lithosphere |
| ILC | −200 | −20 | Into lower crust |
| MML | −100 | −70 | Mid-mantle lithosphere |
| M2UL | −100 | −35 | Mid- to upper mantle lithosphere |
| M2LC | −100 | −20 | Mid-mantle lithosphere to lower crust |
| UML | −70 | −35 | Upper and mid-mantle lithosphere |
| U2LC | −70 | −20 | Upper mantle lithosphere to lower crust |
| LC | −35 | −20 | Lower crust |

Although the effective matrix viscosities $\eta_s$ and$\eta_b$ are functions of $\varphi$ (Schmeling and Wallner 2012), the $\varphi$-dependence of $\eta_s$ has been neglected and $\eta_b$ has been assumed to be 10 $\eta_0$ (i.e., within the CBA, the matrix compacts or decompacts with a constant viscous resistance). These simplifying assumptions are of minor importance because 1 % melt is never exceeded because of melt extraction.

### Extraction and emplacement

As melt is extracted, the corresponding emplacement zone must be defined. We assume that the EZ is bounded by a lower ($z_1$) and upper boundary ($z_2$). Because partial melting usually ascends during the erosional rise of the LAB, it may reach the lower EZ boundary. To avoid extraction and emplacement at the same location, the lower boundary of EZ is defined by the maximum of $z_1$ and the upper front of the extraction region. Thus, the lower EZ boundary depends on the ongoing process. However, the upper boundary of EZ, $z_2$, is fixed. If the extraction front, $\max(z(\varphi = 1\ \%))$, exceeds $z_2$, the EZ has collapsed and the code terminates the run (termination class **E**). It should be noted that this is an unnatural collapse induced by the particular choice of the model setup. More realistic setups at the upper EZ boundary will adjust to the uprising melting front.

Basing arguments on observations to fix the EZ level is hard to find. Different concepts of the evolving lithosphere, e.g., determined by a balanced petrology (phase boundaries) or an evolving LAB, may lead to various approaches. One strategy for solving this ambiguity is to study a model series of systematic EZ variations.

The lowermost lower EZ boundary would formally be the model's bottom, which implies that melt infiltrates the region directly above its original melting region. Disregarding extrusion (or volcanism), the uppermost lower limit would be the mantle–crust boundary because of its large density contrast. The depth range of the upper EZ boundary is assumed to vary from mid-lithospheric level up to the boundary between the lower crust and upper crust.

The presented models are compiled in Table 2, and the corresponding EZ levels are shown in Fig. 3. The EZ of the standard model ILC covers the entire mantle and lower crust from −200 to −20 km.

## Results

To demonstrate the typical physical behavior of a melting-assisted lithospheric erosion model, we first show a selected model run. Remarkable features are the accelerated ascent of the asthenosphere, the erosion of the LAB terminated by a final delamination and the sensitivity of several parameters affecting the viscosity and driving forces, such as the temperature background and anomaly, the density change by enrichment and size and location of the intrusion level (interpreted in "Discussion and conclusions" section). This model will also serve as a standard in the subsequent subsections. Then, other parameters and their sensitivities are discussed in "The influence of other parameters" section. The role of the melt intrusion level will be enlightened presenting the differences due to the variations of the emplacement zone ("Variations of emplacement zone" section).

### Standard model

As the standard model, termed ILC, we define the model with the largest EZ reaching from the top of the melt zone to the boundary between the lower crust (LC) and the upper crust (UC). From the vast amount of calculated data, snapshots of the temperature, melt fraction, melting degree, stress and viscosity fields are compiled for different times to obtain an impression of their interaction and temporal evolution (Fig. 4). The full symmetric fields are plotted to facilitate interpretation, and calculations are only performed for half of them.

A slow, corner-flow-like background flow causes long-wavelength doming of the convecting asthenosphere, as seen in the temperature fields. Local plumes, accompanied by release of melt in the partially molten zones (melt fraction fields) and subsequent emplacement in the EZ (combined depletion and enrichment fields), ascend, and their heads spread under the colder, more viscous lithosphere raising the LAB. Statistically, these plumes most frequently originate above the temperature anomalies at the bottom; however, they are moved along the bottom by sinking lithospheric slabs and spreading drops. Sometimes, the plumes join a single centered plume, and at other times, multiple plumes form away from the anomalies. As the LAB and the melt front ascend and the EZ becomes narrower with time, prominent chimneys with positive feedback develop

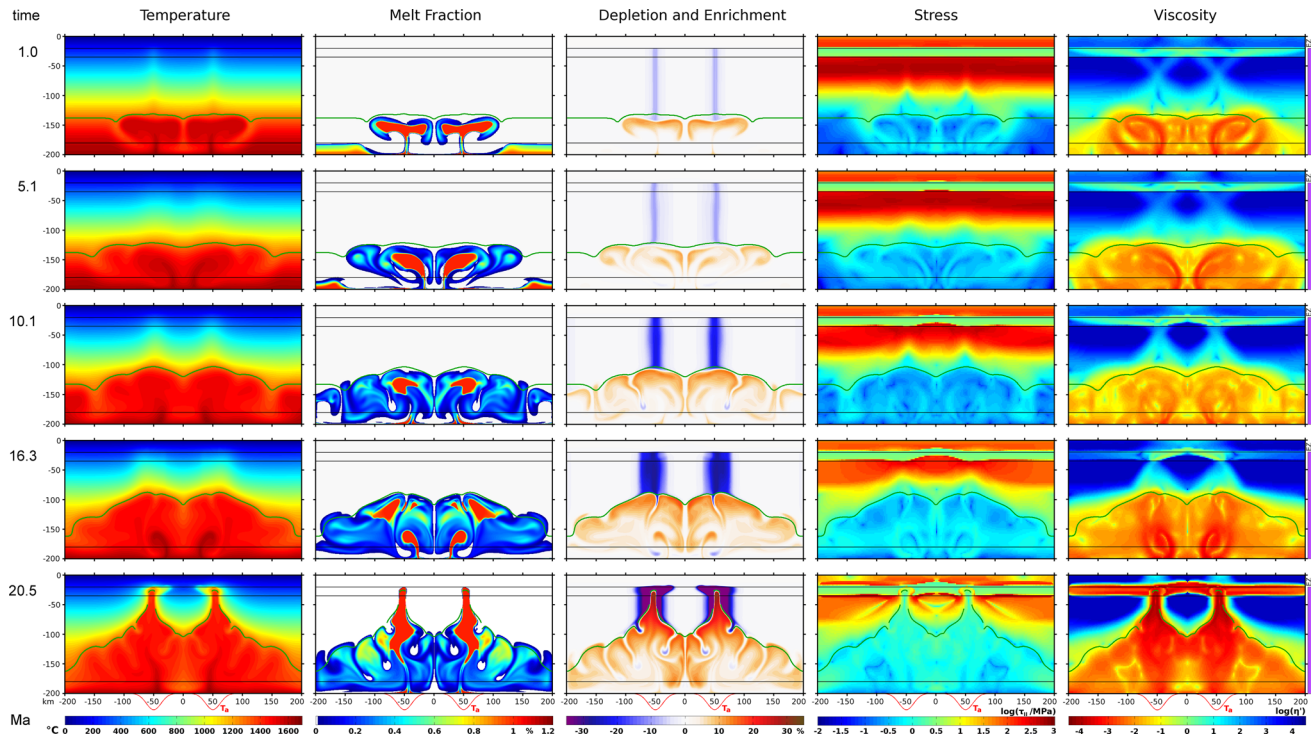


**Fig. 4** Symmetric state fields of model ILC for five selected time steps. Temperature in °C, melt fraction and melting degree (depletion >0 and enrichment <0) in %, second invariant of stress in MPa on a log scale, and logarithm of viscosity scaled by reference viscosity are presented as color maps. For orientation, initial boundaries (crust, LAB) are indicated as *thin black lines*. The transient LAB, which is defined as 80 % of the initial adiabate, is plotted in *green*

and enforce lithospheric erosion. Finally, an asthenospheric break through to the crust occurs, the lower crust fails and the mantle lithosphere begins delaminating (see Wallner and Schmeling 2010, 2011 for a detailed discussion of this characteristic behavior). The positive feedback mechanism, called melt-induced thermal weakening (Schmeling and Wallner 2012), develops when the latent and internal heat associated with extracted melt are transferred to a higher level, which weakens the emplacement region and its vicinity within the mantle lithosphere or even within the lower crust. This weakening reinforces thinning and accelerates advective heat transport because the viscosity is a function of temperature and stress. The excess temperatures in the chimneys reach several hundred kelvin, and the viscosity decreases by one or two orders of magnitude. Extreme values up to solidus and viscosity limits arise with the failure of uppermost mantle lithosphere.

Not only rheological weakening within the enriched zones but also density effects and changes in melting behavior enhance lithosphere erosion and the rise of the LAB. Depletion and partial melting of the source region decrease the density and cause additional buoyancy and convective upwelling. The EZ is heated up and enriched, becoming denser below a depth of 40 km and enforcing downwelling below the LAB. Because these downwellings are displaced sideways with respect to the upwelling, they further contribute to an increasing convective vigor. In addition, depletion and enrichment, combined with temperature changes, affect the melting behavior. Over time, repeated or continuous intrusions combined with continued thinning of the EZ reduce the solidus temperature in the lower part of the lithosphere. Thus, the elevated temperature within the EZ can potentially exceed this solidus. The EZ remelts, as can be seen, between 16 and 20 Ma. Altogether, the rheological weakening of the lithosphere, the increasing convective activity within the asthenosphere and the remelting of the EZ from below accelerate lithosphere erosion.

During early stages, stress in the upper lithosphere reflects the strength resulting from the resistance to extensional lateral outflow. As the viscosity locally decreases, the deviatoric stress evolves into more complex patterns because of its tensor nature and forms shear bands that can be seen in the viscosity fields. Mechanically, the viscosity reduction in the narrow chimneys laterally decouples the central lithospheric block from its surrounding and its vertical mobility increases.

The thermal, melt-assisted erosion of the lithosphere is clearly visible as an updoming of the LAB, which is documented in a sequence of vertical temperature profiles

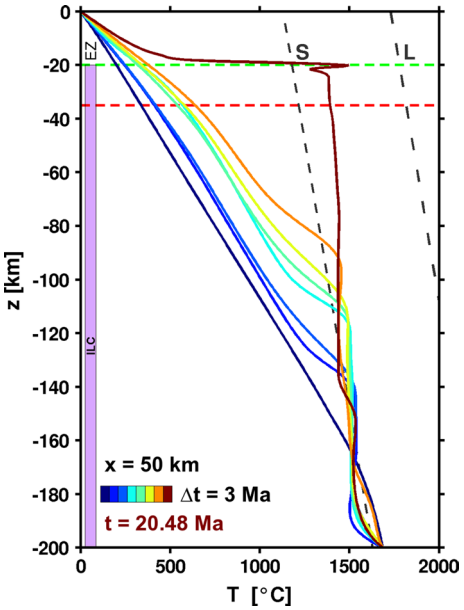


**Fig. 5** Temperature profiles through the *T*-anomaly showing the ascent of LAB of the ILC model for a color-coded time sequence with an interval of 3 Ma. The *T* in the lithosphere increases by several 100 K. The LAB kink continuously rises in pulses. Above a level of −80 km, asthenosphere in the chimneys fast breaks through the strong uppermost mantle

taken at the distance of the anomaly (Fig. 5). The temperature kink, marking the LAB, ascends at a constant rate up to 90 km at 18 Ma. Before delamination, this rise is more irregular and jumping. Furthermore, the temperature at the LAB overshoots the solidus curve more and more during the ongoing process.

### The influence of other parameters

Running a numerical model requires the definition of many physical and technical quantities. To assess the relevance of physical parameters, experience or a sensitivity analysis is necessary. Input data concerning the solid phase, particularly the initial conditions (including the potential temperature, the amplitude and geometry of the temperature anomaly) and the rheology defining the power law and yield strength, have been studied and discussed by Wallner and Schmeling (2011).

One of the most important quantities related to melting is the solidus curve, which may be complex and process-dependent. For simplicity, a linear depth function is applied here (Schmeling and Marquart 2008), and the distance to the liquidus curve is kept constant. The curves are roughly consistent with models of melting of peridotite from Foley et al. (2012, Fig. 13). A basic assumption of our model is the fixing of the anomalous temperature, which results in a few percent of melt at the bottom of the model inside the asthenosphere. Foley et al. (2012) argue for a melt fraction of <5 % at a depth of more than 140 km. Targeting approximately half of this upper limit, the potential temperature was chosen appropriately. Thus, the relationship between the potential temperature and the solidus temperature is more important than their absolute values. Small variations of $T_{pot}$ (of several degrees) do not essentially affect the results.

Variations of the anomaly's excess temperature, $T_a$, from 0 to 200 K have been conducted and reveal a strong control on the temporal behavior, where higher temperatures correspond to faster evolution and finally lead to the termination of class **D** (delamination) or **E** (extraction front reaching the EZ). A clear exponential relationship appears between $T_a$ and the model termination time. In addition, a more physical relationship occurs between the heat flux or Nusselt number and time. Consequently, the lithospheric erosion rate depends on $T_a$. A reduction to half of its value used in the models above decreases the erosion rate by roughly half.

Variations of the fraction limit for melt extraction have a similar influence on the behavior of the model. Although rates and velocities are changing, the principal behaviors of convection and erosion are not affected. A higher melt extraction threshold results in a greater amount of retained melt and increases the vigor of asthenospheric convection, which enhances lithospheric erosion. However, these effects are counteracted by an associated decrease in lithospheric weakening and enrichment, which can slow down lithospheric erosion for the models with deep lower EZ boundaries.

The factor for the density changes due to depletion and enrichment strongly affects the dynamics. Because this factor is only poorly constrained, we varied the value of $\rho_{enr}$ across a range of ±10 % around the value of $\rho_0$. This series revealed a decrease in the LAB erosion as the density contrast becomes smaller. Updoming velocities were reduced by approximately 17 %, independent of the sign of the density contrast. The numbers of slabs and drops with time diminish, the degree of the mixture of originally lithospheric and asthenospheric material decreases, and the irregularity of event peaks as the $v_{RMS}(t)$-function decreases.

Melt flow relative to the matrix follows the Darcy's law, wherein the melt viscosity and permeability determine the material properties. These parameters entered into Eq. (10) via the retention number *Rt* and the porosity exponent *n*. Although the relationship of permeability with porosity is not well constrained for upper mantle conditions and the melt viscosity may deviate from the chosen value of $3 \times 10^2$ Pa s, the two-phase flow has no first-order effect on our results as long as the melt extraction threshold remains small. Therefore, the actual melt fractions are low, and melt

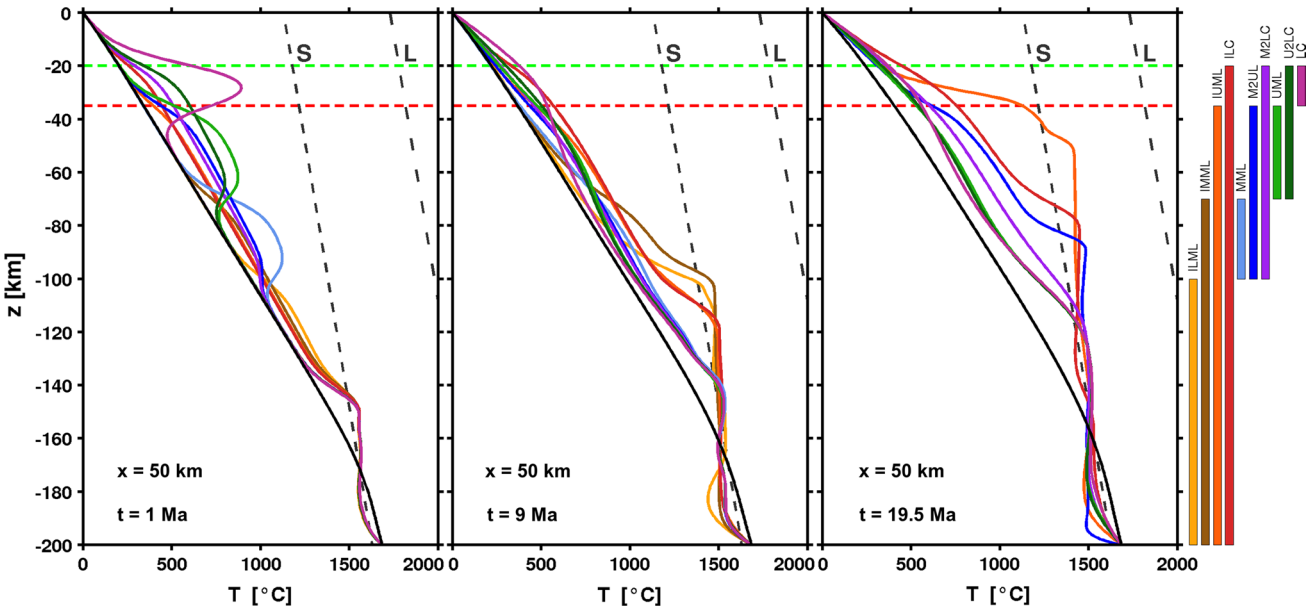


**Fig. 6** Vertical temperature profiles for the EZ model series at the same time points, $T(z, x = 50\ \text{km}, t = [1, 9, 19.5]\ \text{Ma}$, EZs and REF). To compare the effects of the various EZs, the depth profiles of temperature are plotted at the anomaly at the three time points. The models are color coded, with the EZ levels indicated to the *right* and the REF model without melt indicated in *black*. Crustal boundaries and melt curves (S—solidus, L—liquidus) are shown for orientation, and the excess temperatures reach several hundred kelvin. The left-hand and middle graphs show beginning states at 1 and 9 Ma, respectively, when most LAB levels are −140 km or above, and the right-hand graph contains profiles at 19.5 Ma. Here, models ILML, IMML and MML are omitted because they were previously terminated

percolation has a minor influence on the evolution of the models.

### Variations of emplacement zone

The series of systematic variations of EZ depths is listed in Table 2 and shown in Fig. 3. The resulting diverse behavior may allow conclusions on the lithosphere's evolution. The differences in development can be seen when comparing vertical temperature profiles taken above the bottom anomaly (Fig. 6). For comparison, a reference model without melting (REF, black), thus one-phase flow, is added. All profiles begin at $z = -200$ km with the given T-boundary condition of 1686 °C, the anomaly's maximum. Because this temperature is clearly above the solidus (Fig. 3), melt is produced immediately and is extracted as a melting pulse where the extraction limit of melt fraction is exceeded. The thermal evolution of the asthenospheric temperature during the first Ma is the same for all models, and a 50-km-thick convecting layer with supersolidus temperatures above the bottom anomaly develops with a 10-km-thick thermal boundary layer at the bottom. While the differences between the profiles near the model bottom remain small at later times result due to time-dependent convection, they are more pronounced at shallow depths, especially for the LC, UML and MML cases at early times. These anomalies are a consequence of the initial strong melt extraction pulse in combination with the small height of the EZs. If distributed over a wider depth extent of the EZs more broadly distributed, smaller excess temperatures develop (e.g., the brownish curves in Fig. 6, 1 Ma). As time evolves, the initial shallow temperature anomalies of the thin EZ models decay by conduction (Fig. 6, 9 Ma).

Moving upwards, the lithospheric base erosion is visible as a point of transition between the lithospheric and asthenospheric temperature gradients. This erosion is most effective for the models with a deep lower EZ boundary (the four brownish-red I*-models) and occurs because the lower boundary of the EZ is shifted above $z = -150$ km; this boundary is identified by the front of melt extraction. Consequently, the uprising extraction front shortens the EZ, and the intrusional heat distribution becomes more focused (brown curve at 9 Ma or the orange curve at 19.5 Ma). This focusing effect is associated with a temperature increase of more than 500 K and significantly accelerates the rising LAB during the final stage before the collapse of the EZ. This model setup-related collapse of the EZ occurs because the top of the melting zone overrides the fixed top of the emplacement zone and the run is terminated (class **E**).

The melt-free reference model (black curve) shows significantly different behavior. This difference can be understood by considering effective Rayleigh numbers, which can be estimated by multiplying *Rm* and *Rd* by the typical melt fraction (1 %) or degree of depletion or enrichment

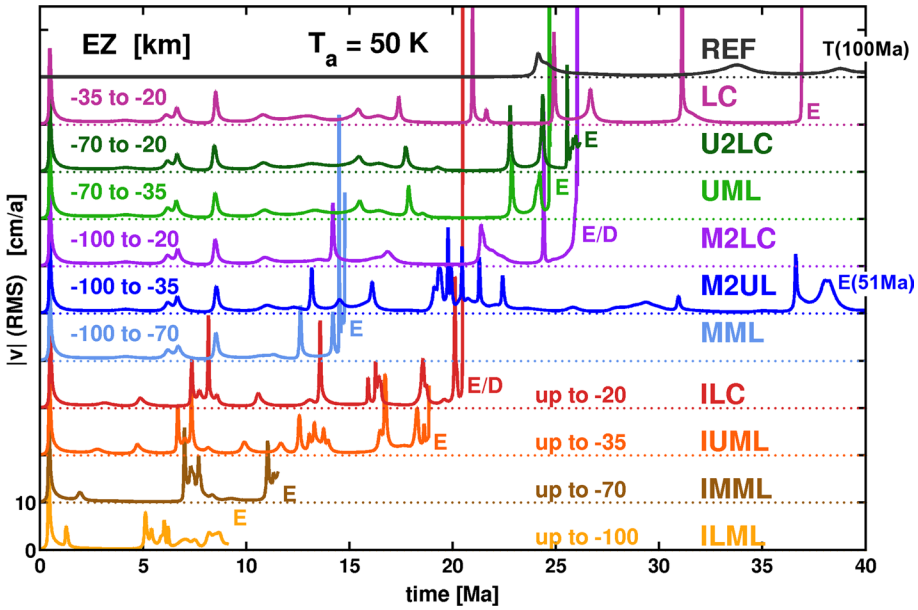


**Fig. 7** Root mean square velocity as a function of time and the variations of the emplacement zone and a "no-melt" reference. Flow events are visible as peaks in the system's RMS velocity. Models are color coded. The emplacement depth ranges are given, and the termination class is noted at the end time. The ordinate scale is valid for the lowest model, and the other scales are shifted by 10 cm/a each, with a *dotted zero line* for reference

(20 %) and inserting the effective thickness of the asthenosphere (50 km) and the effective viscosity ($10^{19}$ Pa s with melt, $10^{20}$ Pa s for the melt-free reference model). The effective depletion and enrichment Rayleigh numbers are on the order of $10^3$–$10^4$, respectively, and the melt Rayleigh number is $<10^3$. In contrast, in the absence of melting, the effective thermal Rayleigh number is <1000, i.e., the asthenosphere is nearly critical or subcritical. Therefore, the melt-free reference model does not convect vigorously, and the LAB rise is strongly delayed.

Models where the LAB kink is well below the lower boundary of the emplacement zone all show a similar temperature increase of approximately 200 K (LC, U* and M2LC at 19.5 Ma). Once the LAB enters the EZ, its rise is accelerated (see also Fig. 9) and the corresponding lithospheric temperature gradient increases. The amplitudes of the excess temperatures are negatively correlated with the actual heights of the EZs. If melt is emplace at shallow depth only (e.g., model LC), the lower part of the lithosphere remains stiff and the lithospheric base erosion is not or is only slightly enhanced. Thus, the depth of the LAB is negatively correlated with the depth of the lower boundary of the EZs.

The root mean square velocity, $v_{\mathrm{RMS}}$, as a function of time characterizes the transient behavior of the entire system. Local flow events, uprising plumes, plunging slabs or falling drops are visible as peaks with amplitudes of 2–20 cm/a (Fig. 7). Two of the ten models (ILC and M2LC) are terminated by delamination (termination class **D** or **E/D**), where $v_{\mathrm{RMS}}$ rapidly rises above 6.5 m/a. The other models are terminated by the EZ collapse (**E**). A common feature of the delamination class models is the high EZ, which ranges into the lower crust. Thus, the central mantle lithospheric block is laterally decoupled from the flanks, and the lower crust central bridge fails. The delaminating models should be regarded as extreme cases.

More commonly, the central lithosphere is eroded or disintegrated by multiple detachment events of drops or slabs, dripping or foundering. Finally, the hanging mantle lithosphere block is too light to cause stresses that are sufficient for causing lower crust failure. The accelerated lithospheric erosion phase (cf. brownish-red curves and light blue curve at 9 and 19.5 Ma in Fig. 6) is characterized by an increase in the frequency of the dripping events compared with the slow erosion case (e.g., model LC, upper purple curve in Fig. 7). In contrast, convection in the melt-free reference model begins at 24 Ma, with first plumes above the *T*-anomaly similar to but weaker than the early plumes of the EZ series, which are observed at approximately 1 Ma.

The differences and effects of the EZ variations are best seen in the field of depletion and enrichment taken at similar times (Fig. 8). A green contour line, defined as 80 % of the initial adiabat, serves as a marker for the transient LAB. Depletion is positive and reddish colored, whereas enrichment is negative and bluish in color. The color bar is limited to 20 % for comparison. Locally higher values are possible, and the given EZ height is shown as a violet bar to the right.

In the first four models (I*), the uppermost $\varphi = 1$ %-front represents the top of the extraction region and simultaneously determines the lower EZ boundary. In model ILML with the deepest upper EZ boundary, the highly enriched regions in the EZ are very narrow. As density increases with the degree of enrichment, heavy slabs plunge beside the plume heads into the weak asthenosphere. The LAB is raised by these and subsequent drops,

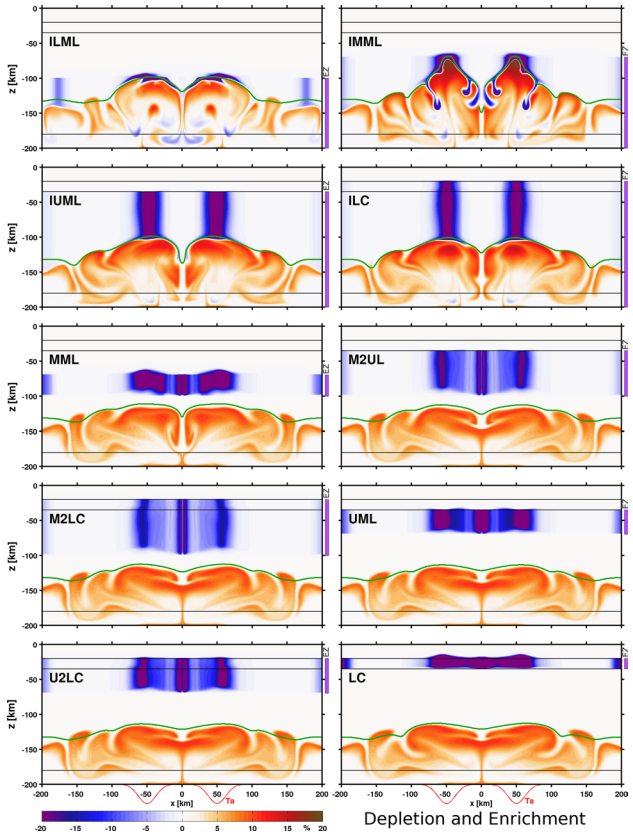


**Fig. 8** Evolution of melting degree fields for the EZ model series. Snapshots of a late stage at approximately 11.5 Ma are tabbed. Depletion is coded in *red* as positive percentages, and enrichment is coded in *blue* as negative percentages. For comparability, the scale is limited to 20 %. The given EZ level is marked by a *violet bar* to the *left*. The bottom *T*-boundary condition (*red*) and the LAB (*green*) are plotted as described in Fig. 4

indicating strong erosion of the lithosphere. In the short chimneys, the melt front rises further, and finally the EZ will ultimately collapse. In the other I* models chimneys of high enrichment concentrations, high temperature, and, in consequence, low viscosity are formed. As their height increases in this model series, the maximum enrichment decreases due to the vertically uniform distribution of the volumetric intrusion rates. Because the corresponding lithosphere is less heated and loaded, the convective activities at the LAB decrease.

In the M*-models, the lowermost lithosphere region between the LAB and the base of the EZ is not affected by the intrusions and thus it is not weakened. Before lithospheric thinning reaches the bottom of the EZ, erosion by asthenospheric convection is less vigorous and not reinforced by slabs driven by an enrichment-caused increase in density. The relatively thin (30 km) EZ of model MML is considerably weakened and, interestingly, the upper EZ boundary, which is originally planar, bulges upward with an amplitude of 10 km.

While a single pronounced chimney develops directly above each temperature anomaly in the I*-models ("$T_a$-chimneys"), which favors localized decoupling, a further central pipe is visible in the M*-models and a central joined plume often forms. Shallower lower EZ boundaries correspond with less intense erosion at the LAB (M*, U* and LC models compared to the I* models in Fig. 8). The high enrichment concentrations in the lower crust result from the phase boundary at −40 km, above which enrichment density causes buoyancy and the degree of enrichment is no longer decreased by downward advection and remelting. The enriched buoyant lower crust is uplifted most significantly in the LC model. This uplift results from rift localization and is assisted by the thermal weakening of the lower crust and increased buoyancy of the enriched material.

## Discussion and conclusions

Our models of a rifting lithosphere have shown that melting is important if melt extraction, fast transport and intrusion are involved. These processes affect the rheology of the lithosphere because they weaken it and accelerate thinning or necking and, consequently, allow erosion of the lithospheric base to occur up to the extreme event of a delamination of the mantle lithosphere.

### Accelerated LAB ascent by melt emplacement

As shown in Fig. 9, the modeled ascent of the LAB within the thinning part of the lithosphere is shown as a function of time for the EZ model series together with a comparable reference model without melt. As expected for the given extensional kinematic boundary conditions, the one-phase reference model REF has an uplift velocity of approximately 1 mm/a or 100 km/100 Ma (shown in the inset). The LC model has the shallowest intrusion zone and is therefore similar to the extrusion of the melt. In addition, the other models with EZ levels inside the lithosphere (M* and U*) show twice the ascent rate as the REF until at least 12 Ma. This effect can be assigned to melt- and depletion-assisted thermal convection within the asthenosphere, while small-scale convection occurs in the REF model.

If the emplacement zones reach down to the melting zone, the rise of the LAB is further accelerated. The efficiency of this process is controlled by the EZ thickness

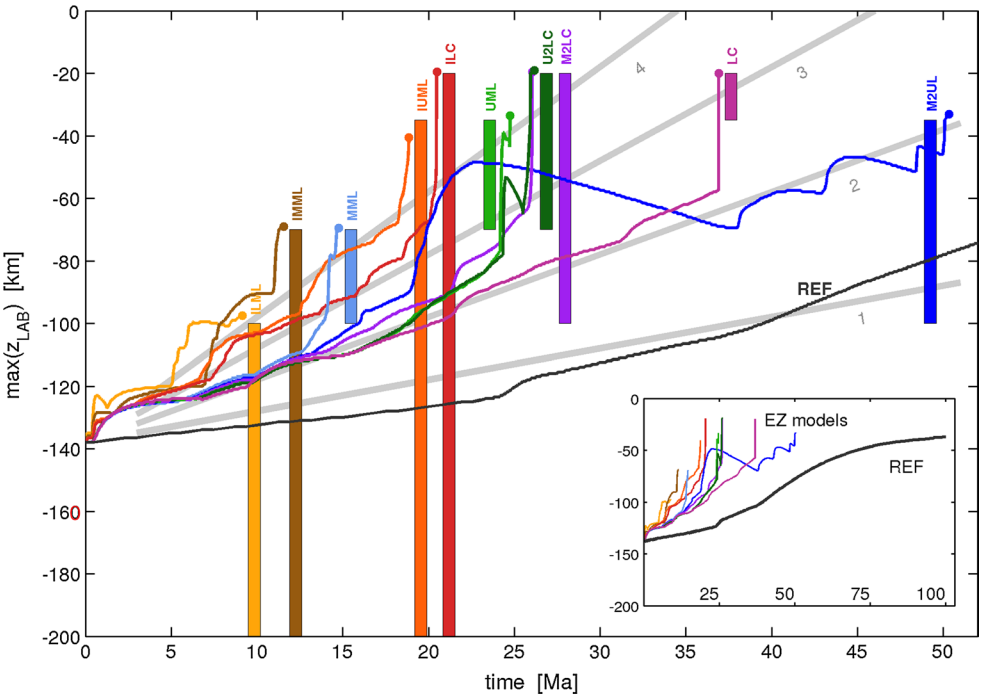


**Fig. 9** LAB ascent for the EZ series and reference model. The depth of the LAB $z_{LAB}(x)$ is defined by the temperature equal to 80 % of the adiabate. The maximum of $z_{LAB}(x)$ (corresponding to the minimum depth of LAB) are plotted as a function of time for each model of the EZ family and a reference model REF. The EZ models are color coded, with REF in *black*. The EZ levels are indicated by *bars*. *Thick gray lines* are used to label orientation rates of 1, 2, 3 and 4 mm/a. The full REF ascent for 100 Ma is shown in an *inset*

and depth location; the increasing depth and narrowness of the zones correspond with more rapid ascent. The causes of this phenomenon are (1) additional buoyancy caused by density changes due to thermal expansion, which results in a temperature increase, (2) dense enrichment destabilizing of the melting zone roof and (3) power-law rheology, where an increase of temperature and stress strongly reduces the viscosity. The regions of melt emplacement are heated by release of the melt's latent and internal heat, and higher effective stress originates from the lateral variations of buoyancy forces.

The relatively fast LAB ascent velocities are episodic. They are associated with plume events as well as intensified melting, while the ascent rate decreases during the interim periods. Several (1–5) pulses at the same or similar locations are necessary to weaken the lithospheric emplacement level and allow the melt front to penetrate until the zone locally collapses (with job termination). The trend of ascent and the termination times of the I* and U* models shows a rate on the order of 4 mm/a. In contrast with this trend, model M2UL is characterized by a more distributed intrusion zone because of the lack of a localized upstream and is associated with repeated plumes.

Clearly, many other parameters (e.g., viscosity law, density contrast, melt extraction limit) and boundary conditions (e.g., extension velocity, for a faster spreading (15 mm/a) see Liao and Gerya (2015)) influence the time behavior of the model. In particular, higher anomaly temperatures increase the speed of the rise of the LAB, as previous tests have shown. However, we restrict this discussion to the effects of extraction and intrusion.

## Continuous erosion versus delamination

The variety of lithospheric erosion styles in the model series ranges from smooth, unbroken and updoming LABs with more or less active convection in the asthenosphere to irregular, broken boundaries where local upstreams intrude and drops and slabs detach and plunge. Ongoing intrusions alter and weaken the lithosphere and increase the tendency for dripping to occur. Due to the release of melt, the ascent of asthenosphere is accelerated and occurs more episodically or pulsating as a sequence of convection events. In a long-term view, this process occurs continuously. However, complete delamination of the mantle lithosphere block requires meeting several special conditions, including a lateral decoupling zone that fully penetrates through the mantle lithosphere, a heavy hanging block that stresses the crust and a susceptible lower crust that can fail. The development of a weak vertical zone depends on the intensity of a temperature anomaly and must not be overly disturbed by asthenospheric convection. The weight of the central block is reduced by erosion from below. If the erosion rate is high, the rest of the block may not build up enough stress to soften the lower crust. In view of these conditions, the delaminating models should be viewed as extreme cases. The delamination conditions are only met in cases M2LC and ILC

(i.e., in cases where the weakening zones of emplacement extend from a great depth within the lithosphere mantle into the lower crust). These two extreme models are consistent with the rift-induced delamination models of Wallner and Schmeling (2010) because their temperature distributions shortly before delamination are similar to the initial conditions of the one-phase flow models studied therein.

### Factors controlling lithospheric erosion

Several factors control the rate of lithospheric erosion: (1) matrix viscosity reduction, (2) accumulating density contrasts by enrichment and depletion causing gravitational forces, (3) reduction of EZ column height by the uprising extraction front, (4) increasing sublithospheric convection. Weakening is enhanced, which increases the mobility at the base of the lithosphere. In the lowermost part of the lithosphere, drops and slabs form, detach and sink into the asthenosphere. This dripping is an expression of an effective erosion. Independent of these melting events, the processes, thinning the lithosphere, are increased by sublithospheric secondary convection, as already shown by Yuen and Fleitout (1985) or Ballmer et al. (2007). The relative importance of the melting-related causes (1)–(3) compared with the thermal erosion (4) alone can be estimated by reviewing the melt-assisted thinning curves with thinning rates of 3–4 km/Ma and the no-melt reference curve with 1 km/Ma. While the latter slow value is influenced by the lack of small-scale convection within the asthenosphere, Yuen and Fleitout (1985) include small-scale convection in their plume-driven lithosphere thinning model and obtain higher thinning rates of 1.4–2.6 km/Ma. Nevertheless, these values are still considerably smaller than our melt-assisted thinning rates, emphasizing the role of the melt. This finding is consistent with a study on the thinning of subcontinental lithosphere that was conducted by Wang et al. (2015). These authors concluded that for the effective erosion of a craton, even at its edge, an additional metasomatic weakening, similar to our "melt-induced weakening," is necessary.

### Influence of enrichment-caused density changes

The enrichment density is not well constrained by petrophysical data, but it may affect the dynamics and flow pattern. Mineralogical estimates of MORB densities have been conducted (e.g., by Irifune and Ringwood (1993) and Irifune et al. (1986)) and suggest that MORB is denser than pyrolite by 110–220 kg/m$^3$ at depths of 200–400 km, or by 50 kg/m$^3$ at a depth of 100 km. Such densities differences cover a range of 1.5–6.6 %. Aoki and Takahashi (2004) measured densities of MORB at various temperatures and obtained a value of 3531 kg/m$^3$ for 1200 °C and a pressure equivalent to 160 km, which corresponded on an increase of 5 % relative to the PREM. Nakagawa et al. (2012) investigated various petrological compositions for the mantle and determined MORB densities with the mineralogical code Perple_X. Roughly between 50 and 150 km, MORB densities strongly increase from 3000 to 3500 kg/m$^3$, covering a range of approximately −5 % to +5 % relative to pyrolite.

Thus, 10 % appears to be an upper bound valid for greater depths. At shallower depths, the effects of enrichment density on erosion may be slightly smaller than modeled. Several tests decreasing the controlling factor from 10 % density increase to 0 or less were performed. Only slightly reduced erosion rates were found.

### Possible role of water

Under the thermodynamic conditions of the earth's upper mantle, small amounts of water have a large effect on the rheology (Karato 2008) as well as on the melt behavior. Due to the high relative solubility of water in melt and the assumed fractional melting, the source rock region may dehydrate and increase its viscosity by one to three orders of magnitude (Hirth and Kohlstedt 1996; Schmidt et al. 2012). On the other hand, contrary to the stiffening effect of dehydration, the emplacement and crystallization of melt increases the water content of the host rock. Depending on composition, temperature and pressure, solubility and fugacity of water, the altered mantle or crustal material is expected to be weakened. This is an additional effect contributing to the viscosity reduction caused by melt intrusion (see also Liao and Gerya 2015).

Erosion of cratonic lithosphere increases the amount of hydrous minerals that infiltrate through the overlying lithosphere, altering the oxidation state and as consequence also the melt curves. Perhaps a change in oxygen fugacity is more important than temperature for melting (Foley 2008).

Hence, because of the complex interrelation of chemical and physical processes of water, melt and rock properties, the effect of water was ignored. However, because water has a strong effect on deformation processes and melting, future modeling should consider the effect of water.

### Models related to findings from the Rwenzori region

This study was motivated by the special situation of the Rwenzori Mountains. The model results are considered in comparison with the observations and their interpretations. In Fig. 10, our view of the recent geological setting is compiled in a section across the Rwenzoris inside the rift system. The deforming lithosphere is structured by seismic discontinuities. Therefore, particularly the melt infiltration

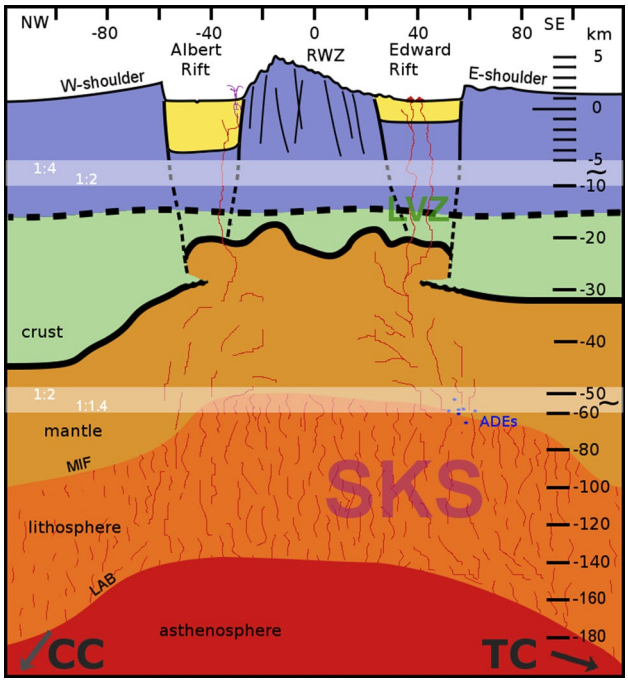


**Fig. 10** Cross section along the profile in Fig. 1 at 3 scales, surface, crust and mantle. High seismicity at −15 km divides the upper and lower crust. The crust–mantle boundary, or Moho, a melt infiltration front (MIF) and the lithosphere–asthenosphere boundary (LAB) are seen with receiver functions (RF). A low-velocity zone (LVZ) in the lower crust is observed by tomography and RF. An earthquake cluster occurring at an anomalous depth of approximately 55 km (anomalous deep earthquake, ADEs) is projected. Rift parallel dikes may explain the anisotropy between the LAB and MIF observed by SKS splitting

front and lithosphere–asthenosphere boundary are of particular interest.

Our approach, which includes "enrichment," is generally consistent with the observations, models and concept presented by Wölbern et al. (2012). Beneath the Albertine rift, the asthenosphere forms a dome between the neighboring cratons with an amplitude of approximately 70 km relative to the 210-km-thick Tanzania craton to the east and the even deeper Congo craton to the west. A network of veins, traces of multiple melt transport events and solidification, alter the lower lithosphere up to the melt infiltration front (MIF). In the Tanzania craton, the MIF discontinuity marks a gradual decay of shear velocity (−12 %) at a depth of approximately 100 km. It climbs toward the rift up to approximately 60 km, becomes sharper, and increases the velocity contrast (−24 %). The mantle-lid above the MIF up to the Moho is denoted as pristine lithosphere, a region not affected by melt infiltration. Further evidence for magmatic intrusions or lenses that are aligned vertical and rift parallel in the lower lithosphere has been furnished by a study on shear-wave splitting by Homuth et al. (2014). These authors observed seismic anisotropy from joint inversion of SKS wave-forms at depths of 60–120 km beneath the Rwenzori region. Another unexpected confirmation of magmatic activity near the MIF discontinuity has come from the detection of mantle earthquakes localized by Lindenfeld and Rümpker (2011).

If we seek to select a best-fitting model from our series and interpret the enriched matrix as altered, infiltrated lithosphere, the MML model (Fig. 8, position 3,1) corresponds well with the data. Near its outer margin ($x = \pm$ 200 km) and within the central region ($-10$ km $< x <$ 10 km), the top of the enriched material is given initially at a depth of $z = -70$ km. Locally, above the $T$-anomaly, chimneys are formed that bulge up to a depth of 60 km. The green line, marking the LAB and mostly coinciding with the melt front, exceeds up to 10 km the level of the lower boundary of the given EZ. If the seismic velocity contrast at the MIF is a measure of enrichment beneath the MIF, then the increase from craton to rift follows an enrichment trend that is consistent with our model.

The next best model that fits the observations was the IMML model (Fig. 8, positions 1, 2), where the extraction front determines the lower EZ boundary. We assumed that the melt emplacement was uniformly distributed over the EZ's height in our model approach. In contrast, in their best seismological as well as petrological velocity models, Wölbern et al. (2012) applied gradients in the altered lithosphere layer. We can regard our step-like distribution function in the MML model as a first-order approximation of a gradient. An adapted distribution function in our models will possibly improve future results. It should further be noted that the model time has not been optimized for comparison (11.5 Ma). The models' minimum LAB depth begins above 140 km and then ascends (Fig. 9), and it should be compared with the shape and amplitude of doming up rather than with the observed depth of 140 km (Fig. 10).

In contrast with the MML model, the intensity of erosion at the LAB in the IMML model is much more pronounced. The maximum rate of asthenosphere updoming is considerably greater (+28 %), and local undulations with a scale of 50 km characterize the LAB. Hence, a survey for such local phenomenon by methods of receiver functions appears infeasible because the smallest diameter of Fresnel zones is 65 km at a depth of 60 km. Moreover, the history of the lithosphere is completely unknown. When the melt front rises up, IMML develops to MML and the models are not distinguishable in a transient stage comparable with recent observations.

To explain the extreme uplift of the Rwenzoris, Wallner and Schmeling (2010, 2011) proposed the possibility of rift-induced delamination of the full mantle lithosphere beneath the mountains. The depth of the LAB proposed by Wölbern et al. (2012) does not confirm that rift-induced

delamination has been fully completed. If it had, we would expect massive volcanism as seen in the characterizing bull's eye pattern. However, the observations agree with the beginning phase of delamination. Independent and recent observations and studies have suggested the occurrence of partial melts in the lower crust, particularly beneath the Lake George region SE of the Rwenzori Mountains (Wölbern et al. 2010; Häuserer and Junge 2011; Jakovlev et al. 2011, 2013; Lindenfeld et al. 2012a), and, furthermore, indications of magmatic activity in the upper crust (Lindenfeld et al. 2012b; Batte et al. 2014). Within the spectrum of parameters studied here, delamination remains an extreme case. However, typical features that correspond to and agree with Wölbern's observations include weakening, erosion, repeated melt intrusions and multiple detachments of blocks from the base of the lithosphere.

**Acknowledgments** We thank an anonymous reviewer and G. Golabek for providing comments and constructive remarks that helped improve our manuscript. In addition, we thank the editor W.-C. Dullo for accepting our manuscript late. We are grateful to members of the RiftLink team for discussions of the Albertine rift, especially Ingo Wölbern, Michael Lindenfeld, and the team around Georg Rümpker, and thank Klemens Link and Steve Foley for providing deep seismological and petrological insights regarding the area beneath the Rwenzoris in the rift and the neighboring cratons. This research was supported by grant Schm872/18-1 embedded in RiftLink project "Rift Dynamics, Uplift and Climate Change in Equatorial Africa" and Schm872/24-1 "The role of magmatic processes for Plume–Craton–Rift Interaction with application to the Tanzania craton and the East African Rift System: A physical approach" from the Deutsche Forschungsgemeinschaft, which is gratefully acknowledged.

## References

Aoki I, Takahashi E (2004) Density of MORB eclogite in the upper mantle. Phys Earth Planet Inter 143–144:129–143. doi:10.1016/j.pepi.2003.10.007

Bahat D, Mohr P (1987) Horst faulting in continental rifts. Tectonophysics 141:61–73. doi:10.1016/0040-1951(87)90174-0

Bajolet F, Galeano J, Funiciello F, Moroni M, Negredo A-M, Faccenna C (2012) Continental delamination: insights from laboratory models. Geochem Geophys Geosyst 13:Q02009. doi:10.1029/2011GC003896

Ballmer MD, van Hunen J, Ito G, Tackley PJ, Bianco TA (2007) Non-hotspot volcano chains originating from small-scale sublithospheric convection. Geophys Res Lett. doi:10.1029/2007GL031636

Batte AG, Rümpker G, Lindenfeld M, Schumann A (2014) Structurally controlled seismic anisotropy above small earthquakes in crustal rocks beneath Rwenzori region, Albertine Rift, Uganda. J Afr Earth Sci 100:579–585. doi:10.1016/j.jafrearsci.2014.08.001

Buck WR (2007) 6.08 Dynamic processes in extensional and compressional settings: the dynamics of continental breakup and extension. In: Watts AB (ed) The treatise on geophysics, vol 6, pp 335–376. doi:10.1016/B978-044452748-6.00110-3

Calais E, Ebinger CJ, Hartnady C, Nocquet J-M (2006) Kinematics of the East African Rift from GPS and earthquake slip vector data. In: Yirgu G, Ebinger CJ, Maguire PKH (eds) The afar volcanic province within the East African Rift System, vol 259. Geol. Soc. Spec. Publ., London, pp 9–22

Chopra PN, Paterson MS (1984) The role of water in the deformation of dunite. J Geophys Res 89:7861–7876. doi:10.1029/JB089iB09p07861

Crameri F, Schmeling H, Golabek GJ, Duretz T, Orendt R, Buiter SJH, May DA, Kaus BJP, Gerya TV, Tackley PJ (2012) A comparison of numerical surface topography calculations in geodynamic modelling: an evaluation of the 'sticky air' method. Geophys J Int 189(1):38–54. doi:10.1111/j.1365-246X.2012.05388.x

Crisp JA (1984) Rates of magma emplacement and volcanic output. J Volcanol Geotherm Res 20(3–4):177–211. doi:10.1016/0377-0273(84)90039-8

Foley SF (2008) Rejuvenation and erosion of cratonic lithosphere. Nat Geosci 1:503–510. doi:10.1038/ngeo261

Foley SF, Link K, Tiberindwa JV, Barifaijo E (2012) Patterns and origin of igneous activity around the Tanzanian craton. J Afr Earth Sci 62(1):1–18. doi:10.1016/j.jafrearsci.2011.10.001

Gerya TV (2014) Precambrian geodynamics: concepts and models. Gondwana Res 25(2):442–463. doi:10.1016/j.gr.2012.11.008

Gerya TV, Meilick FI (2011) Geodynamic regimes of subduction under an active margin: effects of rheological weakening by fluids and melts. J Metamorph Geol 29:7–31. doi:10.1111/j.1525-1314.2010.00904.x

Gregg PM, Hebert LB, Montési LGJ, Katz RF (2012) Geodynamic models of melt generation and extraction at mid-ocean ridges. Oceanography 25(1):78–88. doi:10.5670/oceanog.2012.05

Gummert M, Lindenfeld M, Wölbern I, Rümpker G, Kasereka C, Batte A (2015) Crustal structure and high resolution Moho topography across the Rwenzori region (Albertine rift) from P-receiver functions. Geological Society, London, Special Publications, p 420. doi:10.1144/SP420.4

Häuserer M, Junge A (2011) Electrical mantle anisotropy and crustal conductor: a 3-D conductivity model of the Rwenzori Region in western Uganda. Geophys J Int 185:1235–1242. doi:10.1111/j.1365-245X.2011.05006.x

Hebert LB, Montési LGJ (2011) Melt extraction pathways at segmented oceanic ridges: application to the East Pacific Rise at the Siqueiros transform. Geophys Res Lett 38:L11306. doi:10.1029/2011GL047206

Hirth G, Kohlstedt DL (1996) Water in the oceanic upper mantle: implications for rheology, melt extraction and the evolution of the lithosphere. Earth Planet Sci Lett 144(1–2):93–108. doi:10.1016/0012-821X(96)00154-9

Homuth B, Löbel U, Batte A, Link K, Kasereka CM, Rümpker G (2014) Seismic anisotropy of the lithosphere/asthenosphere system beneath the Rwenzori region. Int J Earth Sci, Albetine Rift. doi:10.1007/s00531-014-1047-0

Huerta AD, Nyblade AA, Reusch AM (2009) Mantle transition zone structure beneath Kenya and Tanzania: more evidence for a deep-seated thermal upwelling in the mantle. Geophys J Int 177(3):1249–1255. doi:10.1111/j.1365-246X.2009.04092.x

Irifune T, Ringwood AE (1993) Phase transformations in subducted oceanic crust and buoyancy relationships at depths of 600–800 km in the mantle. Earth Planet Sci Lett 117:101–110. doi:10.1016/0012-821X(93)90120-X

Irifune T, Sekine T, Ringwood AE, Hiberson WO (1986) The eclogite-garnetite transformation at high pressure and some geophysical implications. Earth Planet Sci Lett 77(2):245–256. doi:10.1016/0012-821X(86)90165-2

Jakovlev A, Rümpker G, Lindenfeld M, Koulakov I, Schumann A, Ochmann N (2011) Crustal seismic velocities of the Rwenzori Region, East African Rift, from local travel-time tomography: evidence for low-velocity anomalies beneath the mountain range. Bull Seismol Soci Am 101(2):848–858. doi:10.1785/0120100023

Jakovlev A, Rümpker G, Schmeling H, Koulakov I, Lindenfeld M, Wallner H (2013) Seismic images of magmatic rifting beneath the western branch of the East African rift. Geochem Geophys Geosyst 14(11):4906–4920. doi:10.1002/2013GC004939

Karato S (2008) Deformation of earth materials: an introduction to the rheology of solid earth. Cambridge University Press, Cambridge. doi:10.1017/S0016756809006323

Katz RF, Weatherley SM (2012) Consequences of mantle heterogeneity for melt extraction at mid-ocean ridges. Earth Planet Sci Lett 335–336:226–237. doi:10.1016/j.epsl.2012.04.042

Katz RF, Spiegelman M, Langmuir CH (2003) A new parameterization of hydrous mantle melting. Geochem Geophys Geosyst 4(9):1073. doi:10.1029/2002GC000433

Kelemen P (2000) Melt extraction from the mantle beneath mid-ocean ridges. Oceanus 41(1):23–28

Kirby SH, Kronenberg AK (1987) Rheology of the lithosphere: selected topics. Rev Geophys 25(6):1219–1244. doi:10.1029/RG025i006p01219

Koehn D, Lindenfeld M, Rümpker G, Aanyu K, Haines S, Passchier CW, Sachau T (2010) Active transsection faults in rift transfer zones: evidence for complex stress fields and implications for crustal fragmentation processes in the western branch of the East African Rift. Int J Earth Sci 99(7):1633–1642. doi:10.1007/s00531-010-0525-2

Koptev A, Calais E, Burov E, Leroy S, Gerya T (2015) Dual continental rift systems generated by plume–lithosphere interaction. Nat Geosci 8:388–392. doi:10.1038/ngeo2401

Lenardic A, Moresi L-N, Muehlhaus H (2003) Longevity and stability of cratonic lithosphere: insight from numerical simulations of coupled mantle convection and continental tectonics. J Geophys Res 108(B6):2302. doi:10.1029/2002JB001859

Liao J, Gerya T (2014) Influence of lithospheric mantle stratification on craton extension: insight from two-dimensional thermo-mechanical modeling. Tectonophysics 631:50–64. doi:10.1016/j.tecto.2014.01.020

Liao J, Gerya T (2015) From continental rifting to seafloor spreading: insight from 3D thermo-mechanical modeling. Gondwana Res 28(4):1329–1343. doi:10.1016/j.gr.2014.11.004

Liao J, Gerya T, Wang Q (2013) Layered structure of the lithospheric mantle changes dynamics of craton extension. Geophys Res Lett 40:1–6. doi:10.1002/2013GL058081

Lindenfeld M, Rümpker G (2011) Detection of mantle earthquakes beneath the East African Rift. Geophys J Int 186:1–5. doi:10.1111/j.1365-246X.2011.05048.x

Lindenfeld M, Rümpker G, Batte A, Schumann A (2012a) Seismicity from February 2006 to September 2007 at the Rwenzori Mountains, East African Rift: earthquake distribution, magnitudes and source mechanisms. Solid Earth 3:251–264. doi:10.5194/se-3-251-2012

Lindenfeld M, Rümpker G, Link K, Koehn D, Batte A (2012b) Fluid-triggered earthquake swarms in the Rwenzori region, East African Rift—evidence for rift initiation. Tectonophysics 566–567:95–104. doi:10.1016/j.tecto.2012.07.010

Link K, Koehn D, Barth MG, Tiberindwa JV, Barifaijo E, Aanyu K, Foley SF (2010) Continuous cratonic crust between the Congo and Tanzania blocks in western Uganda. Int J Earth Sci 99(7):1559–1573. doi:10.1007/s00531-010-0548-8

McKenzie D (1984) The generation and compaction of partially molten rock. J Petrol 25(3):713–765. doi:10.1093/petrology/25.3.713

Mulibo G, Nyblade AA (2013) The P and S wave velocity structure of the mantle beneath eastern Africa and the African superplume anomaly. Geochem Geophys Geosyst. doi:10.1002/ggge.20150

Nakagawa T, Tackley PJ, Deschamps F, Connolly JAD (2012) Radial 1-D seismic structures in the deep mantle in mantle convection simulations with self-consistently calculated mineralogy. Geochem Geophys Geosyst 13:Q11002. doi:10.1029/2012GC004325

Rooney TO, Herzberg C, Bastow ID (2012) Elevated mantle temperature beneath East Africa. Geology 40(1):27–30. doi:10.1130/G32382.1

Saria E, Calais E, Stamps DS, Delvaux D, Hartnady CJH (2014) Present-day kinematics of the East African Rift. J Geophys Res Solid Earth. doi:10.1002/2013JB010901

Schmeling H (2000) Partial melting and melt segregation in a convecting mantle. In: Bagdassarov N, Laporte D, Thompson AB (eds) Physics and chemistry of partially molten rocks. Kluwer Acad., Dordrecht, pp 141–178. doi:10.1007/978-94-011-4016-4_5

Schmeling H (2006) A model of episodic melt extraction for plumes. J Geophys Res 111:B03202. doi:10.1029/2004JB003423

Schmeling H, Bussod GY (1996) Variable viscosity convection and partial melting in the continental asthenosphere. J Geophys Res 101:5411–5423. doi:10.1029/95JB01154

Schmeling H, Marquart G (1991) The influence of second scale convection on the thickness of the continental lithosphere and crust. Tectonophysics 189:281–306. doi:10.1016/0040-1951(91)90502-J

Schmeling H, Marquart G (1993) Mantle flow and the evolution of the lithosphere. Phys Earth Planet Inter 79:241–267. doi:10.1016/0031-9201(93)90150-8

Schmeling H, Marquart G (2008) Crustal accretion and dynamic feedback on mantle melting of a ridge centred plume: the Iceland case. Tectonophysics 447(1–4):31–52. doi:10.1016/j.tecto.2006.08.012

Schmeling H, Wallner H (2012) Magmatic lithospheric heating and weakening during continental rifting: a simple scaling law, a 2D thermo-mechanical rifting model and the East African Rift System. Geochem Geophys Geosyst 13:Q08001. doi:10.1029/2012GC004178

Schmidt P, Lund B, Árnadóttir T, Schmeling H (2012) Glacial isostatic adjustment constrains dehydration stiffening beneath Iceland. Earth Planet Sci Lett 359:152–161. doi:10.1016/j.epsl.2012.10.015

Sobolev SV, Sobolev AV, Kuzmin DV, Krivolutskaya NA, Petrunin AG, Arndt NT, Radko VA, Vasiliev YR (2011) Linking mantle plumes, large igneous provinces and environmental catastrophes. Nature 477:312–316. doi:10.1038/nature10385

Spiegelman M (1993) Physics of melt extraction: theory, implications and applications. Philos Trans R Soc Lond A 342:23–41. doi:10.1098/rsta.1993.0002

Spiegelman M, McKenzie D (1987) Simple 2-D models for melt extraction at mid-oceanic ridges and island arcs. Earth Planet Sci Lett 83:137–152. doi:10.1016/0012-821X(87)90057-4

Šrámek O, Ricard Y, Bercovici D (2007) Simultaneous melting and compaction in deformable two-phase media. Geophys J Int 168(3):964–982. doi:10.1111/j.1365-246X.2006.03269.x

Stamps DS, Calais E, Saria E, Hartnady C, Nocquet J-M, Ebinger CJ, Fernandes RM (2008) A kinematic model for the East African Rift. Geophys Res Lett. doi:10.1029/2007GL032781

Thybo H, Artemieva IM (2013) Moho and magmatic underplating in continental lithosphere. Tectonophysics 609(8):605–619. doi:10.1016/j.tecto.2013.05.032

Till CB, Elkins-Tanton LT, Fischer KM (2010) A mechanism for low-extent melts at the lithosphere asthenosphere boundary. Geochem Geophys Geosyst 11:Q10015. doi:10.1029/2010GC003234

Wallner H, Schmeling H (2010) Rift induced delamination of mantle lithosphere and crustal uplift: a new mechanism for explaining Rwenzori Mountains extreme elevation? Int J Earth Sci 99(7):1511–1524. doi:10.1007/s00531-010-0521-6

Wallner H, Schmeling H (2011) Sensitivity analysis of rift induced delamination with application to Rwenzori Mountains. Geophys J Int 187(3):1135–1145. doi:10.1111/j.1365-246X.2011.05237.x

Wang H, Hunen J, Pearson DG (2015) The thinning of subcontinental lithosphere: the roles of plume impact and metasomatic weakening. Geochem Geophys Geosyst. doi:10.1002/2015GC005784

Weeraratne DS, Forsyth DW, Fischer KM, Nyblade AA (2003) Evidence for an upper mantle plume beneath the Tanzanian craton from Rayleigh wave tomography. J Geophys Res 108(B9):2427. doi:10.1029/2002JB002273

Wölbern I, Rümpker G, Schumann A, Muwanga A (2010) Crustal thinning beneath the Rwenzori region, Albertine Rift, Uganda, from receiver-function analysis. Int J Earth Sci 99:1545–1557. doi:10.1007/s00531-009-0509-2

Wölbern I, Rümpker G, Link K, Sodouti F (2012) Melt infiltration of the lower lithosphere beneath the Tanzania craton and the Albertine rift inferred from S receiver functions. Geochem Geophys Geosyst. doi:10.1029/2012GC004167

Yuen DA, Fleitout L (1985) Thinning of the lithosphere by small-scale convective destabilization. Nature 313:125–128. doi:10.1038/313125a0

Zhong S (2006) Constraints on thermochemical convection of the mantle from plume heat flux, plume excess temperature, and upper mantle temperature. J Geophys Res 111:B04409. doi:10.1029/2005JB003972